33rd Symposium on Naval Hydrodynamics
Osaka, Japan, 31 May - 5 June 2020

Experimental and Numerical Studies of the Flow Around the JBC Hull Form at Straight Ahead Condition and 8° Drift Angle

I. Shevchuk*, A. Sahab, M. Abdel-Maksoud

Hamburg University of Technology, Germany,
* Corresponding author, E-mail: ivan.shevchuk@tuhh.de

ABSTRACT

This paper presents the new experimental and computational data on the JBC (Japan Bulk Carrier) hull form at straight ahead condition and 8° drift angle obtained at Hamburg University of Technology. The experiments were conducted on a double-hull model in a wind tunnel using the PIV technique. Good agreement with the results of other institutions (OU, NMRI) for the straight ahead condition is attained. The simulations at straight course are performed employing two different hybrid approaches, which are compared to each other and to the experimental results in terms of integral and distributed flow quantities. The more reliable approach (SST-DDES - SST-based Delayed Detached Eddy Simulation) is selected for further simulation of the flow at pure drift condition. In all cases a good agreement between the experimental and numerical results for most quantities is observed. However, the numerically predicted TKE levels on fine meshes turn out to be too high compared to the experimentally obtained ones and are attributed to the deterioration of shielding properties of the DDES delay function on finer meshes.

INTRODUCTION

Prediction of the wake quantities for the ships with high block coefficients still remains a challenge for contemporary turbulence models, because of the inherent flow unsteadiness and separations. The main two hull forms which are subjected to intensive investigations in this regard are KVLCC2 and JBC. In the last decade a considerable amount of papers has been devoted to the experimental and numerical studies on KVLCC2 hull form (Ismail, *et al.*, 2009; Xing, *et al.*, 2012; Fureby, *et al.*, 2016). Even though the accurate prediction of its vortex system at high drift angles still remains a challenge (Feder, *et al.*, 2019), reliable predictions of the resistance as well as distributed flow parameters could be achieved using both RANS and hybrid URANS/LES methods at straight course.

The JBC hull form, which is geometrically very similar to KVLCC2, posed a new challenge for the ship hydrodynamics community. Besides the complexities with the prediction of vortex onset and progression at high drift angles, even the predictions of the flow at straight course turned out to be considerably more challenging for CFD methods. Even the most sophisticated RANS models were found to be incapable of predicting the correct levels of TKE in the wake of JBC at straight course (Larsson, *et al.*, 2015), presumably because of stronger large-scale unsteady effects in the stern region. The fact that pure (U)RANS may be unreliable for cases with separations or/and inner flow instabilities was recognized long time ago (Fröhlich & von Terzi, 2008; Spalart, 2000). The understanding, that combination of RANS and LES can at least partly solve the problems of (U)RANS stimulated the usage of hybrid methods in ship hydrodynamics community. Applications of hybrid simulation methods to ship flows have been described in a large amount of research papers in the last years (Xing, *et al.*, 2012; Bhushan, *et al.*, 2013; Fureby, *et al.*, 2016). However, much optimism remained that advanced models like RSTM or EARSM can provide an efficient remedy of the isotropic RANS problems. This can be confirmed by the fact, that for the Tokyo Workshop 2015 only a few research groups performed the computations using scale-resolving approaches, whereas the majority used RANS with models of different levels of complexity (Larsson, *et al.*, 2015). The results of the workshop were surprising: even though the resistance predictions were in most cases very accurate, distributions of velocity and TKE in the wake were accurately captured only by hybrid RANS/LES approaches. This fact provoked more interest from the researchers (Visonneau, *et al.*, 2016; Visonneau, *et al.*, 2018), who continued to investigate the reasons of the (U)RANS failure in some particular cases. At the moment the consensus in the community has been reached, that the vortex systems in the wake of high C_B ships can be much more accurately predicted by some kind of hybrid

RANS/LES or bridging method (e.g. PANS), than by pure (U)RANS. This is the main motivation for application of hybrid methods in the present study.

EXPERIMENTAL INVESTIGATION

The experimental investigation is conducted in the wind tunnel at the Institute of Fluid Dynamics and Ship Theory (FDS) of the Hamburg University of Technology (TUHH). A double model of the JBC is mounted in the wind tunnel on a motion simulator, which provides the required controlled motion.

Facility

The low speed wind tunnel (Figure 1) at TUHH, run by FDS, can operate in either closed or open loop mode. Hence it provides outstanding facility for the investigation of the aerodynamic characteristics of ship superstructures and the investigation of the hydrodynamics of sub-surface objects as well as underwater hulls. The technical data for the test section is shown in Table 1.

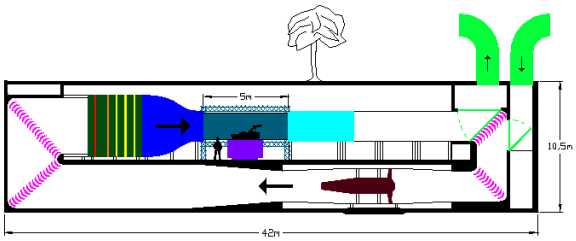

Figure 1: Low Speed Wind Tunnel at TUHH

Table 1: Technical data for test section of the wind tunnel

Dimensions (LxBxH)	5.5m x 3m x 2m
Max. Wind Velocity	35 m/s
Nozzle Contraction Ratio	4.125
Fan Unit Power	400 KW
Turbulence Intensity	$< 0.3\%$
Traversing Mechanism Accuracy	< 0.1 mm

The test section is equipped by a motion simulator (MS) (Figure 2), which consists of eight computer-controlled skids through which the investigated object would be suspended by wires. The skids slide on four rails in a rail-based system, which is equivalent to the linear drive system that was introduced by (Merlet, 2008). The MS can control the six degrees of freedom of the model in predefined trajectories.

The test section allows manual and optical access from the top and the two lateral sides. Positioning of intrusive and non-intrusive measurement sensors is supported by multiple-axes traversing system mounted to the lateral sides of the section. This two-component traverse system is used to move the complete Particle Image Velocimetry (PIV) system for measuring the flow velocity at various planes and positions. Figure 3 shows the model mounted on the motion simulator in the wind tunnel. The PIV system is mounted on the left traverse.

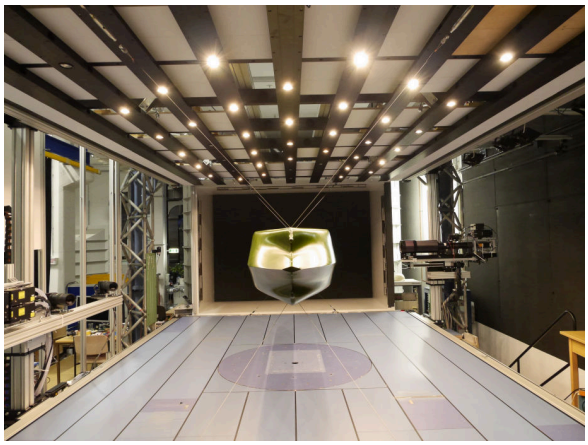

Figure 2: JBC model mounted on the motion simulator with PIV system on the right traverse

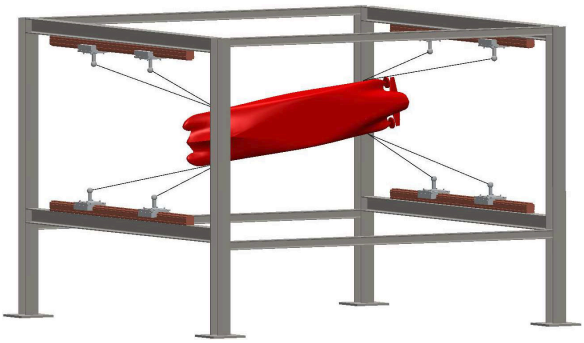

Figure 3: Motion Simulator Schematic

Ship Model

For the experimental investigations in the wind tunnel, a double body model of the underwater hull of the JBC is used in which the hull is mirrored around the selected waterline. The main parameters of the ship in comparison to the model are shown in Table 2.

Test Conditions

An inflow air velocity of 10m/s is used for both the straight ahead and pure drift tests. The air tempera-

Table 2: Main parameters of the ship and the model

Symbol	Unit	Ship	Model
L_{oa}	[m]	291	3.651
L_{pp}	[m]	280	3.513
B	[m]	45.2	0.565
T	[m]	16.6	0.208
C_B	[-]	0.848	0.848
λ	[-]	1	79.7
S	[m^2]	$2.0 \cdot 10^4$	3.135

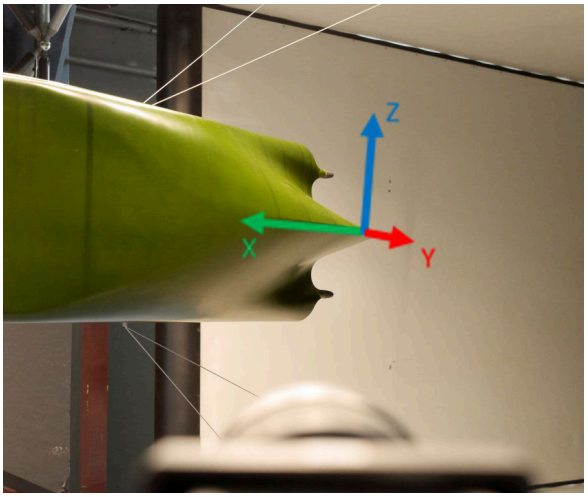

Figure 4: JBC-Model coordinate system

ture during the measurements is tracked to determine the Reynolds number. Due to the negligible temperature variation, the Reynolds number can be considered constant at 2.42×10^6. The model is restrained from all free motions by fixing it to the motion simulator.

In the pure drift measurements, a drift angle of 8° is used, which is obtained through adjusting the orientation of the model with the motion simulator. The blockage ratios of the wind tunnel were 0.04 and 0.06 for the straight ahead and pure drift measurements respectively. Zigzag stripes are used on the model bow for turbulence stimulation and their positioning is selected according to ITTC recommendations at $1/3$ of the bulb length of the bulbous bow from its fore end, at $5\%L_{pp}$ aft of the Forward Perpendicular (FP) and at shortly before the expected position of the positive pressure gradient approximately $8.8\%L_{pp}$ aft of FP (ITTC, 2017).

Measurement Techniques

Particle Image Velocimetry System

The spatial distribution of the velocity components in different planes is measured by a modular commercial 2D-3C-PIV system of TSI Inc. The stereoscopic PIV system (SPIV) consists of a pulsed laser, a light sheet optic, two cameras and a computer with software to control image generation and processing.

The light sheet is generated by a 200 mJ two-head Nd-YAG-laser (Quantel Big Sky). Scattered light is received by two PowerView 4M (2048x2048 pixel, 12bit, monochrome) cameras equipped with 105mm/F2.8 lenses; their baseline is located approximately 1.7 m from the middle of the test section. The optical axes of the lenses are inclined 61° and 44° to the normal of the laser plane.

In order to avoid blur caused by the oblique view of the cameras, a rotatable base adjusts the angle between the lens and CCD chip to satisfy Scheimpflug condition. The cameras record two images each with a short time separation (Δt=25μS). In order to reach sufficient signal-to-noise ratio for the subsequent image processing and to minimize the loss of pairs, the time separation should be selected to meet the condition that a particle would travel nearly 25% of the light sheet thickness.

For the PIV measurements, particles of an average diameter of about 1 μm are generated as the seeding. The Laskin type droplet generator uses Di-Ethyl-Hexyl-Sebacat (DEHS). The generator is placed downstream of the test section. The fog generated spreads through the wind tunnel at a closed loop operational mode and leads to a global seeding. Therefore, any influence due to turbulence of the generated fog is negligible.

The images are analysed by means of a FFT-transformation, cross correlation technique and ensemble averaging of the calculated correlation maps. Gaussian curve fitting is applied to estimate the location of the correlation peak with sub-pixel accuracy. No pixel locking effects has been recognized. The results are calculated with a 50% overlap of neighbouring vectors for the two-component vector maps of each camera. Reconstruction of three component velocities is based upon the vector maps of both cameras as well as calibration data.

The calibration is executed by capturing a set of images for a calibration target. A black calibration target with a predefined rectangular grid of dots spread on two planes will be used to capture the calibration images. The required calibration data is calculated by evaluating these images. The calibration of the PIV system is sensitive to even small changes of the geometrical and optical configuration. Therefore, the whole PIV-components are installed on one crossbar. Then the crossbar can be moved by the traversing mechanism in vertical and horizontal di-

rection.

Data Acquisition

CFD computations were used for determining the approximate location of the vortices and then define the positions of the measuring planes. The location of the measurements stations are shown in Figure 5. The exact positions are shown in Table 3. The PIV measurements in the straight ahead condition as well as the pure sway are conducted for the two stations S4 and S7, while seven stations are investigated at the pure drift condition. In order

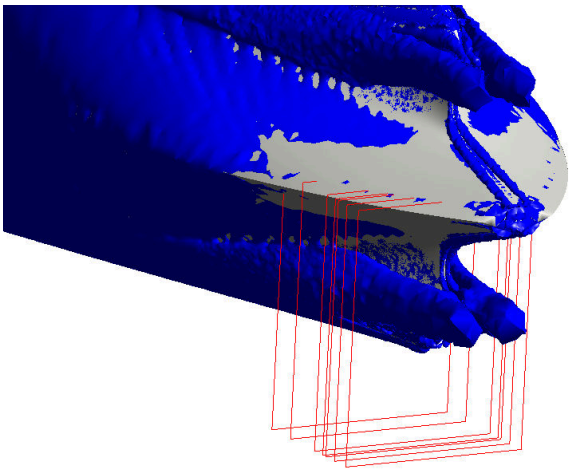

Figure 5: Measurement planes

to enhance the final output of the measurements and to avoid peak locking, focused images with high resolution are captured at each measuring station. The focused images are captured at 15 predefined positions so that they form a 5x3 matrix (i.e. 5 rows and 3 columns of images).

The offset between images is selected to maintain a sufficient overlap between neighbouring images. At each of the 15 positions for all measuring stations, 1000 images were recorded. The overlap algorithm produces the final full image by constructing a grid with a grid offset that is equivalent to the grid offset of each of the individual positions to prevent any aliasing effects.

Data Reduction

The velocity components are calculated by using the full set of data. In order to calculate the velocity fluctuation, the set of data is divided into 20 smaller subsets of 50 images each. The mean velocity components for these 20 sets are calculated and then used to determine the velocity fluctuation around such mean value. The velocity components U_i and the velocity fluctuation components u_i are computed using:

$$U_i = \frac{1}{N}\sum_{k=1}^{N} U_{i,k} \tag{1}$$

Table 3: Measurement stations for straight ahead (SA) and pure drift (PD) conditions

Plane	x_s[mm]	x_s/L_{pp}[-]	SA	PD
S1	175.7	0.05		x
S2	131.7	0.0375		x
S3	74.3	0.0211		x
S4	55.2	0.0157	x	x
S5	47.8	0.0136		x
S6	27.1	0.0077		x
S7(AP)	0.0	0.0000	x	x

$$u_i = \frac{1}{N}\sum_{k=1}^{N} (U_{i,k} - U_i) \tag{2}$$

where the index i = 1, 2 or 3 indicate the axial, traverse and vertical velocity components (U,V,W) for U_i and velocity fluctuation (u,v,w) for u_i. The index N represents the collected data for every interrogation area. The turbulent kinetic energy k is computed using the Reynolds normal stresses as follows:

$$k = \frac{1}{2}(uu + vv + ww). \tag{3}$$

The derivatives of the velocity components are used to compute the vorticity vector components as:

$$(\omega_x, \omega_y, \omega_z) = (\frac{\partial W}{\partial y} - \frac{\partial V}{\partial z}, \frac{\partial U}{\partial z} - \frac{\partial W}{\partial x}, \frac{\partial V}{\partial x} - \frac{\partial U}{\partial y}). \tag{4}$$

UNCERTAINTY ASSESSMENT

The PIV system is mounted on a crossbar, 2D automated traverse system. The same configuration was earlier used in conducting PIV measurements on KVLCC2 model (Abdel-Maksoud, *et al.*, 2015) and therefore it is safe to assume that the same uncertainty assessment still applies. The uncertainty of the positioning is ± 0.1 mm. The estimated uncertainties of the three velocity components are $W = \pm 0.08$ m/s, $V = \pm 0.06$ m/s and $U = \pm 0.33$ m/s. The relative uncertainties of the velocity components to the free stream velocity are $W = \pm 0.80\%$, $V = \pm 0.60\%$ and $U = \pm 3.30\%$.

The uncertainty of the 2D automated traverse system was estimated based on a high number of repetition tests. The uncertainties of the measured data by the PIV system are determined based on the dimensions of the measuring planes and the resolution of the used cameras as well as the selected time shift between two images. Each measuring plane has about 50% overlap area with its neighbours.

COMPUTATIONAL INVESTIGATION

Turbulence modeling

Formulation of hybrid RANS/LES momentum and continuity equations

The hybrid methods, used in the present work are based on the well-known RANS equations, in which the turbulent (hybrid) viscosity is locally adapted to the cell size; therefore the basic equation system has the common formulation:

$$\frac{Du_i}{Dt}+\frac{1}{\rho}\frac{\partial p}{\partial x_i}=\frac{\partial}{\partial x_j}\left[(\nu+\nu_t)\left(\frac{\partial u_i}{\partial x_j}+\frac{\partial u_j}{\partial x_i}\right)\right]+f_i \quad (5)$$

$$\frac{\partial u_i}{\partial x_i}=0 \quad (6)$$

Here p and $\mathbf{u}$ are the hybrid pressure and velocity, ν - kinematic viscosity and ν_t - hybrid viscosity. The definition of hybrid quantities can be given using the concept of effective filter (Fröhlich & von Terzi, 2008; Sagaut, *et al.*, 2013). The described below hybrid RANS/LES turbulence models differ in the way, how the hybrid viscosity is calculated.

DDES

Delayed Detached Eddy Simulation is one the most well-known hybrid RANS/LES models. Its first version was based on the Spalart-Allmaras one-equation RANS-closure (Spalart, *et al.*, 2006). Later, a different version of the model was proposed (Gritskevich, *et al.*, 2011), which is based on SST model of Menter. The governing PDEs of the model are as follows:

$$\frac{\partial k}{\partial t}+u_j\frac{\partial k}{\partial x_j}=\frac{\partial}{\partial x_j}\left[(\nu+\sigma_k\nu_t)\frac{\partial k}{\partial x_j}\right]+\widetilde{\mathscr{P}}_k-k^{3/2}/l_{DDES} \quad (7)$$

$$\frac{\partial \omega}{\partial t}+u_j\frac{\partial \omega}{\partial x_j}=\frac{\partial}{\partial x_j}\left[(\nu+\sigma_\omega\nu_t)\frac{\partial \omega}{\partial x_j}\right]+ \quad (8)$$

$$2(1-F_1)\sigma_{\omega 2}\frac{1}{\omega}+\frac{\partial k}{\partial x_j}\frac{\partial \omega}{\partial x_j}+\frac{\gamma}{\nu_t}+\widetilde{\mathscr{P}}_k-\beta\omega^2$$

$$\nu_t=\frac{a_1 k}{\max(a_1\omega,F_2 S)} \quad (9)$$

Where $\widetilde{\mathscr{P}}_k$ is the limited production term, which reads: $\widetilde{\mathscr{P}}_k=\min(\nu_t\overline{S}^2,10\beta^* k\omega)$. The turbulent viscosity should be understood as the hybrid viscosity here, F_1 and F_2 are the SST blending functions, whereas $\sigma_k,\sigma_\omega,\beta^*$ and a_1 are the model constants, their values can be found in (Gritskevich, *et al.*, 2011). The hybrid length scale is a combination of the RANS and LES ones, given by the following expressions:

$$l_{DDES}=l_{RANS}-f_d\max(0,l_{RANS}-l_{LES}) \quad (10)$$

$$l_{LES}=C_{DES}\Delta \quad (11)$$

$$l_{RANS}=\frac{k^{1/2}}{\beta^*\omega} \quad (12)$$

$$C_{DES}=C_{DES1}F_1+C_{DES2}(1-F_1) \quad (13)$$

$$\Delta=\Delta_{\max} \quad (14)$$

$$f_d=1-\tanh([C_{d1}r_d]^{C_{d2}}) \quad (15)$$

$$r_d=\frac{\nu+\nu_t}{\kappa^2 y^2\sqrt{0.5(S^2+\Omega^2)}}. \quad (16)$$

Here κ is the von Karman constant, y - wall distance, S,Ω - magnitudes of the strain rate and vorticity tensors respectively. A complete description of model constants and the set of shielding functions can be found in (Gritskevich, *et al.*, 2011) and omitted here, since exactly the same model formulation was used.

Dynamic DDES

This model was proposed by (Yin, *et al.*, 2015) and is based on the DDES, but some considerable changes were made. First of all, instead of the SST model, this DDES formulation is based on the Wilcox's $k-\omega$ model. Second of all, the mechanism of hybrid viscosity reduction works differently: instead of the increase of the destruction term for k in the LES region, its production term is decreased. This is achieved by the redefinition of the turbulent viscosity. The model equations read:

$$\frac{\partial k}{\partial t}+u_j\frac{\partial k}{\partial x_j}=\frac{\partial}{\partial x_j}\left[(\nu+\sigma_k\left(\frac{k}{\omega}\right)\frac{\partial k}{\partial x_j}\right]+2\nu_t S^2- \quad (17)$$

$$C_\mu k\omega$$

$$\frac{\partial \omega}{\partial t}+u_j\frac{\partial \omega}{\partial x_j}=\frac{\partial}{\partial x_j}\left[(\nu+\sigma_\omega\left(\frac{k}{\omega}\right)\frac{\partial \omega}{\partial x_j}\right]+2C_{\omega 1}S^2- \quad (18)$$

$$C_{\omega 2}\omega^2$$

$$\nu_t=l_{DDES}^2\omega \quad (19)$$

The hybrid length scale is again a combination of the RANS and LES ones, but in a DDES manner:

$$l_{DDES}=l_{RANS}-f_d\max(0,l_{RANS}-l_{LES}) \quad (20)$$

$$l_{RANS}=\frac{\sqrt{k}}{\beta^*\omega};l_{LES}=C_{DES}\Delta;\Delta=f_d V^{1/3}+(1-f_d)\Delta_{max} \quad (21)$$

The shielding function corresponds to that of the original DDES formulation:

$$f_d=1-\tanh([C_{d1}r_d]^{C_{d2}});r_d=\frac{\nu_t}{\kappa^2 y^2\sqrt{U_{i,j}U_{i,j}}} \quad (22)$$

where $U_{i,j}$ is the velocity gradient tensor. In the original formulation of Yin et al. the constants of the shielding function were $C_{d1} = 8, C_{d2} = 3$, but for the simulations conducted in the present study $C_{d1} = 20$ was used in order to strengthen the shielding. The value of the constant is found for each cell locally, using the dynamic procedure, similar to the Lilly's modification of the dynamic Smagorinsky model:

$$C_{dyn}^2 = 0.5 \frac{L_{ij} M_{ij}}{M_{ij} M_{ij}} \tag{23}$$

$$L_{ij} = -\widehat{\overline{u_i} \overline{u_j}} + \widehat{\overline{u_i}} \widehat{\overline{u_j}} \tag{24}$$

$$M_{ij} = \widehat{\Delta}^2 \widehat{\overline{\omega}} \widehat{\overline{S}}_{ij} - \Delta^2 \widehat{\overline{\omega} \overline{S}_{ij}} \tag{25}$$

In order to avoid the application of the dynamic procedure in the flow regions with coarse mesh resolution, a limiter for the C_{DES} is introduced, based on the Kolmogorov length scale and the characteristic cell size:

$$C_{DES} = \max(C_{lim}, C_{dyn}) \tag{26}$$

$$C_{dyn}^2 = \max(0, 0.5 \frac{L_{ij} M_{ij}}{M_{ij} M_{ij}}) \tag{27}$$

$$C_{lim} = C_{DES}^0 [1 - \tanh(\alpha e^{\frac{-\beta \Delta_{max}}{L_k}})] \tag{28}$$

$$C_{DES}^0 = 0.12, L_k = (\frac{\nu^3}{\varepsilon})^{\frac{1}{4}} \tag{29}$$

Again, the complete set of model constants and the implementation details is omitted here, but can be found in (Yin, *et al.*, 2015).

RANS/LES interface

It is well known, that hybrid RANS/LES models have an issue at the interface between RANS and LES regions. This issue is usually referred to as grey area problem. It consists in the lack of resolved turbulence in the LES region right after the switch from RANS and sometimes results into the physically inadequate behaviours. Examples of such behaviours are the modelled stress depletion (MSD), grid induced separation (GIS) and log-layer mismatch (LLM). The first one is the reduction of the modelled stresses near the body (which is not compensated by resolved ones), the second one consists in a premature separation given the local mesh refinement and adverse pressure gradients. The LLM is a mismatch of the velocity profiles in the logarithmic region of the boundary layer at the interface between RANS and LES. In modern versions of the hybrid methods (such as previously described DDES) the mentioned problems are much less pronounced, because special treatment was applied (delay function in DDES, empirical blending functions and the LES length scale in IDDES). Therefore when the models are carefully used, most of the issues can be avoided. Later, however, two other ways in which the grey area problem can manifest itself were described in literature (Mockett, *et al.*, 2015; Menter, 2016). One of them is the insufficient DDES shielding in case of the flow with adverse pressure gradient or/and mesh refinement and the other one - slow transition to resolved turbulence in the free shear layers. The latter drawback is the reason, why the dynamic DDES model is used in the current study. As experience shows, this model provides a much faster transition from RANS to LES in the separated regions, than DDES and at the same time still has a DDES-type shielding in the attached boundary layer.

Wall treatment

In all the computations the equations are integrated to the viscous sub-layer. The wall functions are applied only in the regions with the insufficiently fine wall-resolution on the area of 0.2-0.3 % of the ship surface and therefore should not play any considerable role for the presented results.

Discretization

The simulations described in the present paper are conducted using the OpenFOAM software. For the solution of the equations (6) the PISO algorithm is used. The maximum Courant number in the computational domain is set to 0.85, so that the resolution of vortex dynamics could be achieved. The discretisation of the convective terms in the momentum equation was done using the second order hybrid scheme, proposed by (Strelets, 2001). The convective terms in the auxiliary equations (k, ω) were discretised using TVD scheme of van Albada. For the discretisation of the laplacian operator in all equations (incl. pressure eqn.) second order centred scheme with non-orthogonal correction was used. The gradient approximation was done using hybrid Green-Gauss/weighted least-squares method (Shima, *et al.*, 2013).

Mesh generation

The meshes for the computations are generated using the `snappyHexMesh` generator from the OpenFOAM library. It is notorious for having problems in generation of the prism mesh in the boundary layer. Therefore, some ad-hoc modifications to the meshing algorithm were made, which allowed for 99.7% coverage with the prism layers with the average y^+ value of 0.8. Three unstructured hex-dominant meshes: g3 (3.1M), g2 (8.1M) and g1 (22.4M) cells were generated by refinement of the base cell size by 1.41. This way a uniform isotropic cell size of 0.20, 0.14 and 0.10% of the L_{pp} is attained at the ship surface and in the wake (except for the prism layers). In the local refinement regions the cell sizes are 0.1, 0.07, 0.05% of the

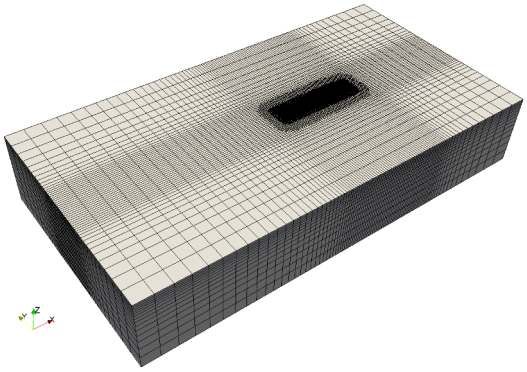

Figure 6: Structure of the computational mesh

L_{pp} respectively. No refinement of the FSV vortex core was performed therefore the sizes of the cells in the vortex core depend on the location of the vortex. In the finest regions, where the vortex lies close to the ship hull the ratio of the Taylor microscale to the cell size $\lambda_g/\Delta x$ ranges from ≈ 2 on g3 to ≈ 1 on g1. In the coarsest regions this ratio by far exceeds the presented values.

The example of the mesh structure is shown in Figure 6. The sizes of the computational domain (length x breadth x height) were: $6L_{pp}$ x $3.2L_{pp}$ x $1.0L_{pp}$. These sizes were used for all considered cases (straight ahead motion, pure drift, sway). The symmetry plane was located at z=0 and corresponded to the one in the experiment.

The computations in each case are conducted in the following manner. First, the steady-state computations using the underlying RANS models are conducted (either k-ω SST or Wilcox's k-ω) till convergence. After that the hybrid computation (dynamic DDES or DDES) is started. In order to avoid any influence of the transition from RANS to hybrid solution on the results, the period of time of $\frac{L_{pp}}{U}$ (which corresponds to 0.35s) is excluded from the statistics, so that the analysed interval is $[1\frac{L_{pp}}{U}, 4\frac{L_{pp}}{U}]$.

RESULTS

Straight Ahead

Flow description

The flow in the stern region of JBC is dominated by 4 vortices: two primary and two secondary counter-rotating ABV vortices. While the primary vortices are induced by the flow around the bilge of the after-body, the secondary vortices are generated by the cross-flow below the stern bulb. After the onset of the primary ABV the boundary layer rolls up into it and is then being transported downstream, so that the low velocity regions can be see left and right from the stern bulb (see Figure 21). In Figure 22 ($x/L_{pp} = 0.05$) one can see the generation of the ABV upstream from the stern bulb region and the generation of the secondary vortices at $x/L_{pp} = 0.0$, which are considerably smaller and decay very fast, so that already at section $x/L_{pp} = -0.03$ they cannot be seen any more.

The high values of the TKE are concentrated near the boundary layer - mostly at the ship bottom, whereas in the core of the vortex a minima can be seen (Figure 23). Obviously the strong turbulence from the hull boundary layer, which is being sucked into the vortex, is not reaching the vortex core and remains in the shear layer surrounding it (section x/L_{pp} = 0.05).

In Figure 24, showing the pressure field, one can see a superposition of a classic high pressure region at the stern due to flow deceleration and two large low pressure regions in the cores of ABVs. Additionally, smaller pressure minima and maxima can be seen due to the secondary vortices.

Comparison of experimental results to other institutions

The velocity components u_x, u_y and u_z are measured with the PIV system at both stations as illustrated in Figures 31 to 33 and 36 to 38. Based on the velocity components, the vorticity and turbulent kinetic energy are calculated as illustrated in Figures 34 to 35 and 39 to 40 .

The results of the new measurements are compared to the data provided by the National Maritime Research Institute (NMRI) and University of Osaka (OU). Both the NMRI and the OU measurements were conducted in a towing tank with the Reynolds numbers $7.46{\cdot}10^6$ and $2.17{\cdot}10^6$ respectively. The comparison is carried out for two stations: S4 and S7. The propeller axis is unfortunately partially blocking the field of view of the cameras at the selected stations and thus the results show one half of the JBC model. This effect is comparably insignificant at S7. The comparison of the experimental results for the TKE is shown in in Figures 7 and 8 and for the axial velocity and vorticity Figures 53 to 56 and

Even though the OU and NMRI measurements were conducted at different *Re*, the isolines of the axial velocity in the proximity of the center line are in good agreement with each other. The TUHH measurements were conducted on a double-hull model at *Re*, very close to that considered by OU, but narrower isocontours are observed, than both in OU and NMRI results above the stern bulb and in the region of ABV. Due to the incompressibility condition this also leads to stronger velocity deficit below the stern bulb. This difference is probably due to the effect of the stern wave crest as well as trim and sinkage, which create additional adverse pressure gradient in the stern region, leading to faster boundary layer growth. This phenomenon is present only in towing tank measurements and absent in wind tunnel experiments. Similar effects of

the free surface were also reflected in some of the computations, presented for Tokyo Workshop (Deng, *et al.*, 2015).

At the same time, the isolines in the outer region of the wake agree well between OU and TUHH results, whereas NMRI results show narrower outer contours. The reason may be the dependence of the overall wake width on the Reynolds number.

An important difference in the results between OU, NMRI and TUHH is that OU and NMRI measurements showed u_x minima of 0.2-0.3 in ABV vortex region and 0.2 below the stern bulb, whereas TUHH measurements don't show velocity minima in this region and the minima below the stern bulb is considerably lower: 0.1. At the section S7 the same overall trends can be observed.

At the section S4 the contours $\omega_x = 50$ are in good agreement among all institutions. The maxima of $|\omega_x| = 100$ near the core of the ABVs are present in TUHH and NMRI results, but could not be captured in OU measurements. Due to the stronger velocity deficit under the stern bulb in TUHH measurements, the values of vorticity are significantly higher and reach $100 - 150$.

Besided the ABV, the vorticity field at S7 reveals the presence of the small counter-rotating vortices near the symmetry plane below the stern bulb. The structure of the ω_x field agrees perfectly between TUHH and NMRI results, however, in the TUHH measurements the vortices seem to be considerably wider. The fact that the vorticity field at S4 and S7 shows asymmetry in some regions, despite averaging, means, that a long-period fluctuations of the vortices below the stern bulb are present.

For the turbulence kinetic energy the following trends can be noticed. In the outer region the isoline $k = 0.005u_\infty^2$ stretches higher upwards in OU results, than in TUHH results, where the high TKE is concentrated under the stern bulb and is not propagating so much upwards. The location of the maxima is the same, but with different values: 0.01 for OU and 0.03 for TUHH. Higher values of the TKE are due to stronger vorticity under the stern bulb.

The TKE values at S7 in TUHH measurements decrease, compared to S4. The maxima is reduced to 0.02. In the OU results an opposite trend can be noticed, where the maxima increases from 0.01 to 0.025. At the same time, the location of the maxima is similar and shifted to the right from the symmetry plane. In TUHH results the high TKE region is thin and concentrated near the vorticity maxima, whereas in OU results the distribution is more uniform. It seems, that the long-period fluctuations of vortices, mentioned earlier also lead to considerable asymmetry of the TKE field in TUHH results, where the high TKE region is "rotated" about the stern bulb by few degrees.

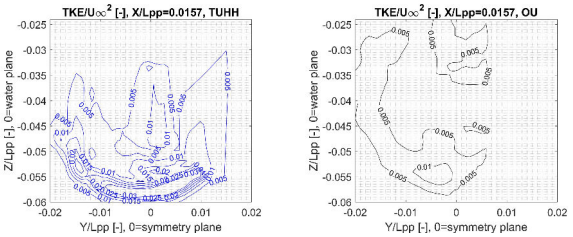

Figure 7: TUHH (left), OU (right) results for TKE at S4

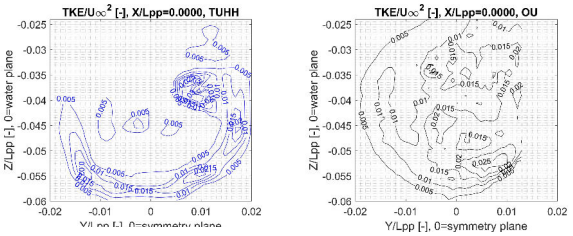

Figure 8: TUHH (left), OU (right) results for TKE at S7

Dynamic DDES

Convergence of forces The resistance of the considered model was not measured during the experiments, therefore the comparison of the computed and experimental values for the resistance is not possible. Nevertheless in order to analyse, how the mesh refinement influences the forces, the averaged values of the total resistance as well as of its components were computed. They can be seen in Table 4. It can be easily noticed, that the values of the total resistance and of its components are showing either a monotonic or oscillating divergence. However, the oscillation amplitude is not too high: the difference between the minimum and the maximum values equals approximately 5% of C_T obtained on g3.

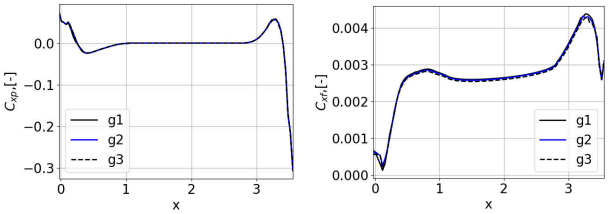

(a) (b)

Figure 9: Average force coefficient for hull sections along the x-coordinate (100 bins were considered). (a) - Pressure force, (b) - Friction force

The following reasons may lead to the observed behaviour: the use of unstructured grids and change of the model behaviour in response to mesh refinement. In order to check the first hypothesis, computations on the structured grids are required.

Comparison of the flow fields to experimental results In Figures 41 to 46 one can see the comparison between the experimentally obtained velocity components, vorticity and TKE fields and the ones obtained during the simulations on different grids: coarse (g3), medium (g2) and fine (g1). The total TKE was found as the sum of the half of the trace of the resolved Reynolds stress tensor and the modeled TKE. In order to restrict the volume of the presented graphical information only sections S4 and S7 are presented. For the u_x, u_z and ω_x fields a very good quantitative and qualitative agreement between the experiment and the simulations can be observed. Most importantly, the mesh refinement brings positive improvement to the computational results for these fields. The anchor-like structure in the u_x field is reproduced very well, especially on the coarse and fine grids. It seems that the grey area problem is at strongest on the medium mesh. The contours and the values of the vertical velocity the experimental and computational results are very similar, even though in the former a considerable noise is still present. One can observe, how the reduction of the modeled TKE and the numerical diffusion leads to the increase of the vorticity levels in the ABV vortex center. On the fine grid the experimental and numerical values are very close, which means that the vortices are much less diffused than on the coarse mesh. For the transverse velocity component and the total TKE the agreement with the experiment is unfortunately worse. Some of the features of the flow are smeared out on the fine grid, even though on the coarse grid they are present. For example the local extrema of u_y near the stern bulb are almost completely smeared out in the computation. The mesh refinement brings no considerable improvement in this regard. The extrema of ω_x near the stern bulb, which are present on the coarse mesh also vanish on the finer meshes. The situation with the TKE is as follows. On the one hand computation on the coarse mesh reproduced the geometric structure of the TKE field which is almost identical to that observed in the experiment, but the levels are largely underestimated. On the other hand the levels of the TKE on the medium and fine meshes correspond much better to the experimentally observed ones, but the size of the highly turbulent regions is considerably larger.

Table 4: Convergence of resistance coefficients at straight course for various simulation approaches,TUHH

	g1	g2	g3
RANS			
C_T	4.62E-03	4.59E-03	4.58E-03
C_P	1.10E-03	1.12E-03	1.14E-03
C_F	3.52E-03	3.48E-03	3.43E-03
DDES			
C_T	4.72E-03	4.56E-03	4.55E-03
C_P	1.23E-03	1.10E-03	1.13E-03
C_F	3.49E-03	3.46E-03	3.42E-03
Dyn.DDES			
C_T	5.65E-03	5.38E-03	5.56E-03
C_P	1.76E-03	1.64E-03	1.60E-03
C_F	3.89E-03	3.74E-03	3.96E-03

Discussion of the model behaviour In order to better understand, why for some quantities the solution on the fine mesh was worse than on the coarse one, one has to first compare the location of the RANS/LES interface between the different grids. As can be seen in Figure 10, there is a rapid change in location of the interface between the coarse and medium mesh.

On the medium and fine meshes, the interface is obviously shifted into the boundary layer (which is an unexpected behaviour of the model) and therefore the model is working in an intermediate mode between DDES and WMLES. The fact, that the interface is located inside the boundary layer for the grids g2 and g1 triggers the generation of the resolved turbulence (which can be seen in Figure 14) before reaching the wake region. At the same time, it is obvious, that the adequate resolution of the vortices in the boundary layer would require much finer grid, than the one used in present computations. Therefore physical adequacy of the "naturally" generated turbulence in the attached flow is at least questionable. The fact that

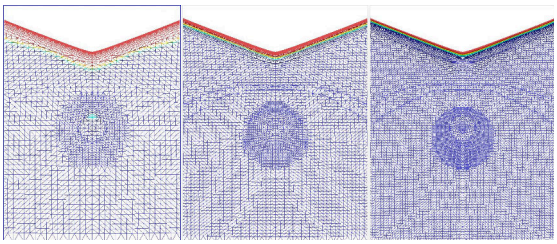

Figure 10: RANS/LES distribution at the section x/L_{pp}=0 for coarse (left), medium (center) and fine (right) meshes

the model switched to SRS inside the boundary layer also raises concerns regarding the accurate prediction of the mean velocity profiles. In order to check the influence of the interface on the velocity distribution in the boundary layer, the velocity profiles along the line perpendicular to the ship bottom at $x/L_{pp} = 0.5$ were compared (see Figure

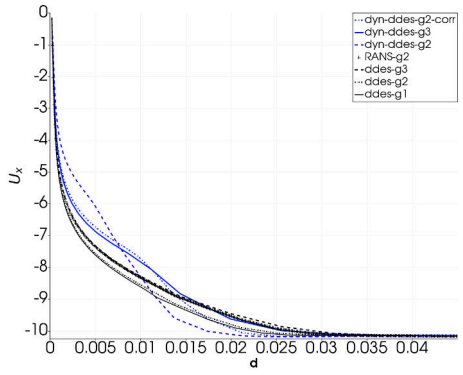

Figure 11: Comparison of the mean velocity profiles in the boundary layer on the ship bottom for different resolutions and methods

11). Here, the RANS solution is considered as a reference one, since RANS can much better predict the growth of attached boundary layers (Spalart, 2000) and the separation. Obviously, already on the coarsest grid the shielding of the dynamic DDES model is not capable of preserving the correct velocity profile. On the medium grid (g2) the result deteriorates further, the boundary layer becomes much thinner, than predicted by RANS. This, of course, makes the prediction of the wake less accurate. Obviously the velocity gradient becomes higher under these conditions, which may be the reason for the high levels of the TKE, observed in the wake. At the same time high levels of the TKE mean stronger turbulent transport, which leads to smearing out of some flow features on the medium and fine meshes.

The conducted analysis shows, that the shielding function of the dynamic DDES model cannot as is provide sufficient shielding of the attached boundary layers. The intention of the application of this model was to allow the solution to more rapidly switch to resolved turbulence after the separation and by these means to reduce the gray area in the wake. It seems that the mitigation of the gray area problem in the wake comes at the cost of the inaccurate prediction of the flow quantities in the attached boundary layer.

Therefore further modifications of the model or application of other models are needed, which would provide the sufficient shielding in the attached boundary layers and rapid transition to resolved turbulence in the wake region. In order to partly address this issue, the computations with the original SST-DDES model, were conducted too. The results of DDES will be presented in the following subsections.

DDES

The aim of application of DDES was to check, if this model would show better results and prevent smearing of flow features and incorrect prediction of the velocity in the near-wall region. Since in case of DDES the C_{DES} constant is not adapted to the flow (i.e. not reduced), the shielding function is supposed to be strong enough to prevent generation of (under)resolved turbulence at the ship hull. This hypothesis can be verified by checking the presence of the turbulent vortices in the attached region of the boundary layer (see Figure 15). Obviously the spontaneous generation of resolved turbulence is suppressed in this case and the boundary layer remains shielded from LES.

Comparison of the flow fields to experimental results The comparison of the flow fields obtained from DDES to the experimental ones is shown in Figures 31 to 40. For the coarse and medium meshes a considerable improvement of the results has been attained, compared to dynamic DDES approach. The distribution of the velocity components, longitudinal vorticity and TKE agree much better with the experimental results. The sizes and the form of the wake are predicted more accurately and the flow features (like isolines) show consistency between the meshes - they don't vanish or show rapid changes. However, as soon as the mesh is refined further, the solution seems to change considerably. Even though the agreement of velocity components and vorticity in section S4 is still good, the prediction of other quantities and in other sections has become much worse. For example, the TKE in section S4 showed rapid increase in the entire region near the stern bulb, which points to the dramatic increase of the resolved turbulence production. This again (similar to dynamic DDES results) led to smearing out of the flow features, which can be seen in section S7 for the velocity components and vorticity. The observed phenomenon however has a different explanation than that given for dynamic DDES solution. Analysis of the solution in the stern region showed, that on the the fine mesh the grid-induced separation takes place and the separation bubble appears below the stern bulb at approximately x/L_{pp} = 0.068. In this region strong velocity fluctuations are present which lead to high resolved TKE production. The reason for velocity fluctuations is the effective change of the flow topology because of the separation bubble (see Figure 13).

Convergence of forces Because of the effect described in the previous paragraph, the force convergence could not be attained. The values of resistance coefficients on the coarse and medium meshes are very close to each other, but due to the GIS the pressure force coefficient has in-

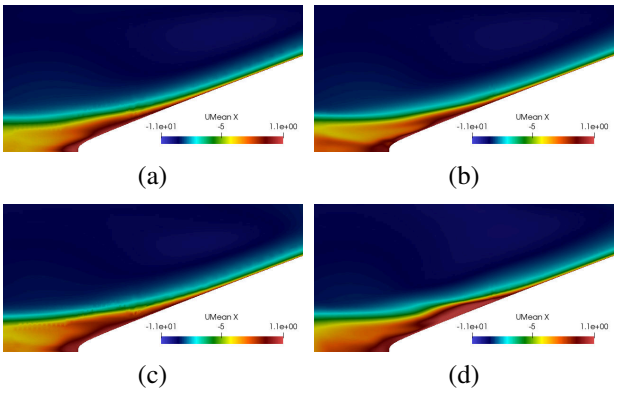

(a) (b)

(c) (d)

Figure 12: Separation bubble at the stern region in different computations: (a) - coarse mesh, RANS; (b) - fine mesh, RANS; (c) - coarse mesh, DDES; (d) - fine mesh, DDES

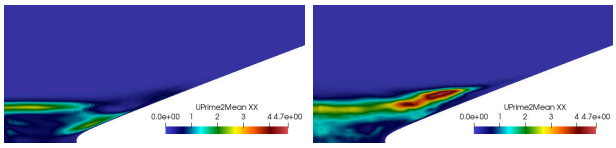

(a) (b)

Figure 13: Reynolds stress $\langle u_x'^2 \rangle$ on (a) - medium mesh, (b) - fine mesh

creased by approximately 10% on the fine mesh. Generally, the coefficients are much smaller than that predicted by the dynamic DDES model (see Table 4).

Pure Drift

Flow description

The flow at pure drift motion is dominated by the complex vortical structures. Some of them are shedding from the fore body (fore-body side vortex) and some of them from the after-body (ABV). The FSV sheds from the bilge of the forward shoulder and the boundary layer on the ship's bottom is fed to the vortex. The low pressure on the leeward side stimulates the development of the vortex formation. Similar flow characteristics take place on the after shoulder on the leeward side and result in the aft-body bilge vortex. One can also notice a number of other vortices in the wake, which strongly interact with each other but we will not focus on these.

FSV is generated in the boundary layer, but quickly leaves the boundary layer region and the interaction between them is rather weak. The progression of FSV takes place in the outer flow region and not influenced by the boundary layer. However, the global pressure variations change the trajectory of the vortex center in the after part of the ship. On the contrary, the propagation of ABV takes place in the wake of the ship and there is a strong interaction with the ship boundary layer especially coming from the ship sides.

The Figure 26 shows the interaction between the boundary layer and ABV, which lead to high TKE values in the proximity of the vortex core (see Figure 28). whereas FSV is just slightly affected by it. The low values of TKE in FSV, presented in the Figures may be not physically correct due to the lack of resolved turbulence structures in the vortex core, since no additional refinement boxes were used for it. The vortex cross-section in the outer region was resolved with just 5 to 6 computational cells. In Figure 27 one can see that the strength of ABV is significantly higher than that of FSV in the stern region.

Convergence of forces

The coefficients of the forces, acting on the model at pure drifting motion are shown in Table 5. Unlike the total resistance of the model at straight course, most of the coefficients show either monotone or oscillating convergence. Keeping in mind, that the same meshes and same numerical schemes were used for both cases, one can conclude, that the modelling error does not play such a significant role for the forces at the drifting motion as for the straight ahead condition.

Table 5: Convergence of forces/moments coefficients for drift motion, TUHH

	g1	g2	g3
$C_{T,x}$	5.28E-03	5.14E-03	4.70E-03
$C_{P,x}$	1.70E-03	1.57E-03	1.13E-03
$C_{F,x}$	3.57E-03	3.57E-03	3.57E-03
$C_{T,y}$	1.21E-02	1.15E-02	9.53E-03
$C_{P,y}$	1.19E-02	1.13E-02	9.26E-03
$C_{F,y}$	2.58E-04	2.68E-04	2.69E-04
$m_{T,z}$	9.41E-03	9.34E-03	9.17E-03
$m_{P,z}$	9.23E-03	9.16E-03	8.99E-03
$m_{F,z}$	1.77E-05	1.80E-05	1.79E-04

Comparison of the flow fields to experimental results

In Figures 47 to 52 one can see the comparison between the experimentally obtained velocity components, vorticity and TKE fields and the ones obtained during the simulations on different grids: coarse (g3), medium (g2) and fine (g1). As for the straight course,

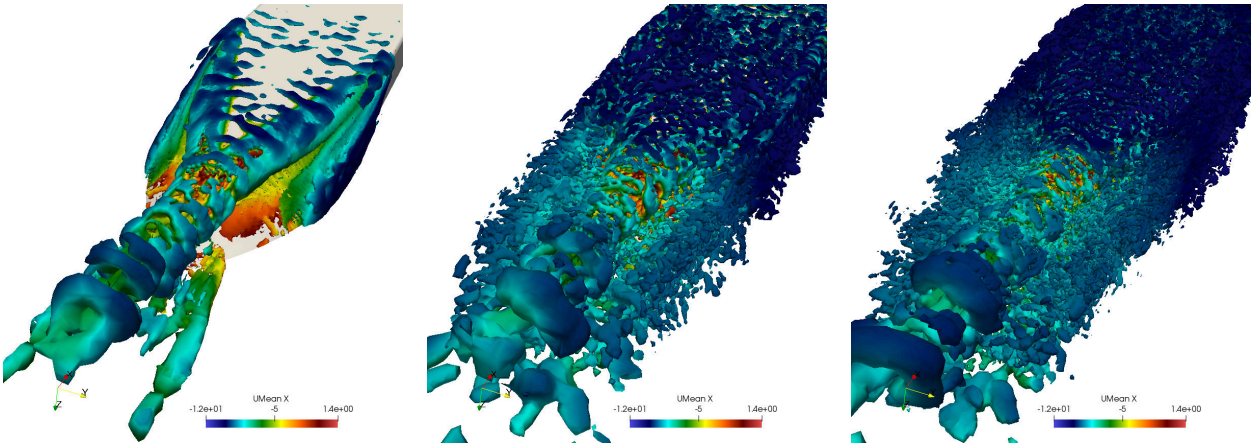

(coarse) (medium) (fine)

Figure 14: Comparison of the instantaneous vortex structures ($Q = 200$) at the stern for different meshes at straight ahead motion. Dynamic DDES (Yin, *et al.*, 2015)

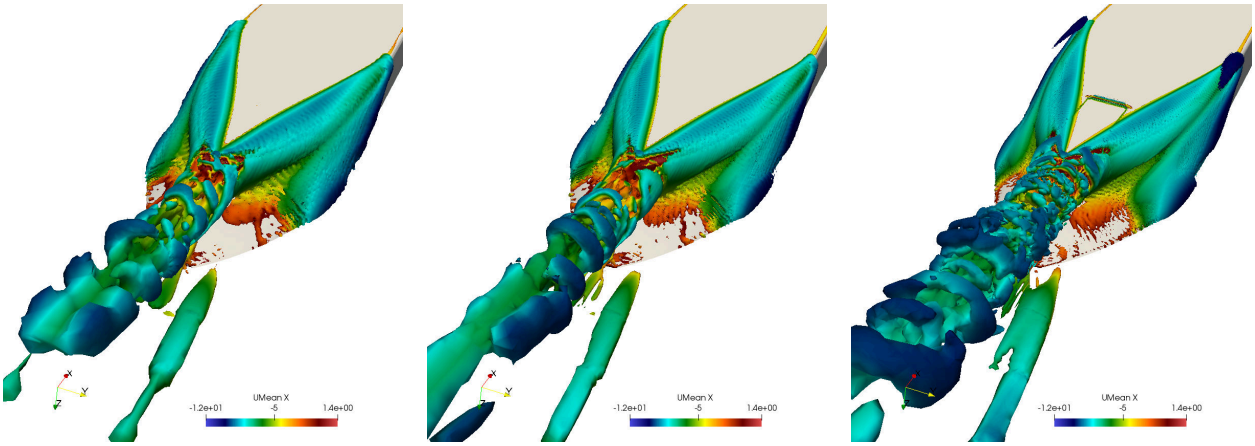

(coarse) (medium) (fine)

Figure 15: Comparison of the instantaneous vortex structures ($Q = 200$) at the stern for different meshes at straight ahead motion. DDES (Gritskevich, *et al.*, 2011)

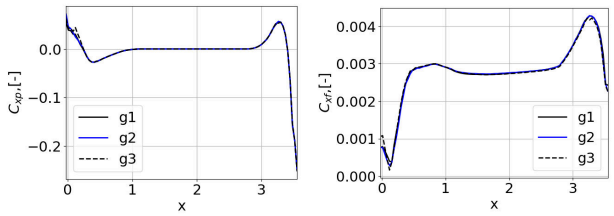

(a) (b)

Figure 16: Average force coefficient for hull sections along the x-coordinate (100 bins were considered). (a) - Pressure force, (b) - Friction force

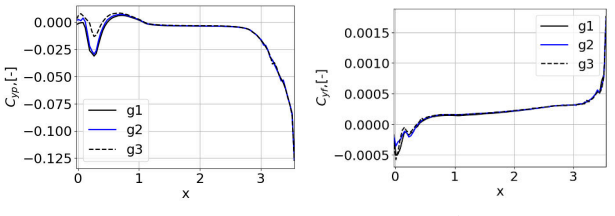

(a) (b)

Figure 17: Average force coefficient for hull sections along the x-coordinate (100 bins were considered). (a) - Pressure force, (b) - Friction force

the total TKE and the modeled TKE are shown. In order to limit the volume of the presented graphical information only the results for the sections S4 and S7 are presented.

For the u_x field qualitative and quantitative agreement between the experiment and the simulations

can be observed. However, the backflow region at the middle line plane seems to be too large in the simulation. The contours agree well with the experimentally observed ones. However, even on the fine mesh the ABV vortex seems to be much broader, than in experimental results.

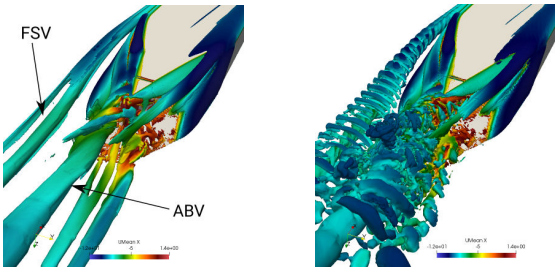

Figure 18: Vortex system in the wake of JBC hull. (a) - Time averaged, (b) - Instantaneous

The u_y and u_z are also predicted very well: all the main features seem to be correctly captured by the model. The values of ω_x increase when the mesh is refined due to lower numerical and model diffusivity. However, the same phenomenon is unfortunately observed on the fine mesh as for the straight course. Namely, the flow features are smeared out and very high TKE levels are observed - neither the form, nor the values of the TKE field are predicted correctly.

This means, that application of DDES can be problematic even in case of drift, where strong flow instabilites are expected.

Analysis of the quantities in the vortex core

Grid convergence and comparison to experimental data

Using the method of Sujudi-Haimes (Sujudi & Haimes, 1995) the vortex center lines of the FSV and ABV vortices (see Figure 18 for details) were extracted from the computed flow fields (see Figures 19, 20). The flow quantities were sampled along these lines for both vortices.

As for the FSV vortex both the vertical and horizontal position of it are almost independent of the mesh resolution - only small oscillations can be observed among the meshes, nevertheless the vortex center line coordinates on the fine and medium meshes are almost identical, which indicated grid convergence.

The values of the vorticity are, as expected, higher on the finer meshes. At the same time the rate of decay seems to be independent of the mesh resolution. Again a trend to grid convergence can be seen.

Prediction of the TKE and the u_x inside the vortex seem to be more problematic, the behaviour of these quantities change more noticeably between the meshes and in some regions grid divergence is observed (see e.g. Figure 19(d), x/L_{pp} from -0.2 to 0.1, where a rapid growth of TKE on the fine mesh can be seen). However, in integral sense, the difference between the curves obviously become smaller as the grid is refined.

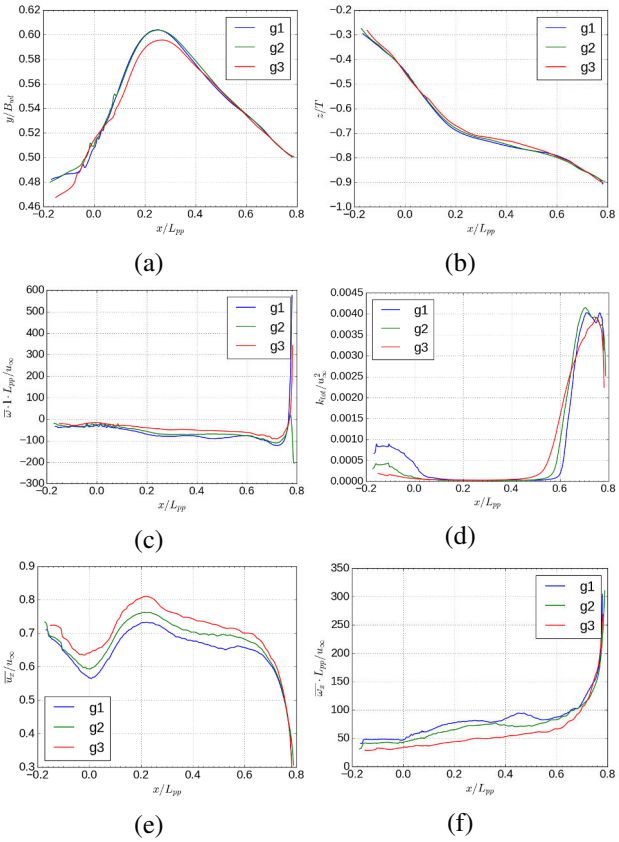

Figure 19: Sampling of the flow quantities along the vortex center for FSV: (a),(b) - y, z coordinates respectively, (c) - vorticity about the vortex center line ($\boldsymbol{\omega} \cdot \mathbf{l}$), (d) - total TKE, (e) - axial velocity, (f) - axial vorticity

For the ABV vortex also the experimental values are available, so also the conclusions on the model predictive capability can be drawn. One can see that the vertical and horizontal positions of the ABV vortex center are predicted accurately and show trend to grid convergence in the region $x/L_{pp} \in [0; 0.15]$, however in the wake region the convergence could not be attained. The discrepancies of about 5% with experimental values can be seen, which can be considered a good result for the distributed quantities. The distribution of longitudinal velocity along the vortex core does not show agreement with the experimental values - in some points the values are overpredicted by 30%. The data scatter is very large. At the same time the values of the vorticity seem to be in a good agreement with the experimentally observed ones on the medium and fine meshes. As for the TKE levels, they are in satisfactory agreement. The TKE value in the ABV vortex center line also show grid convergence.

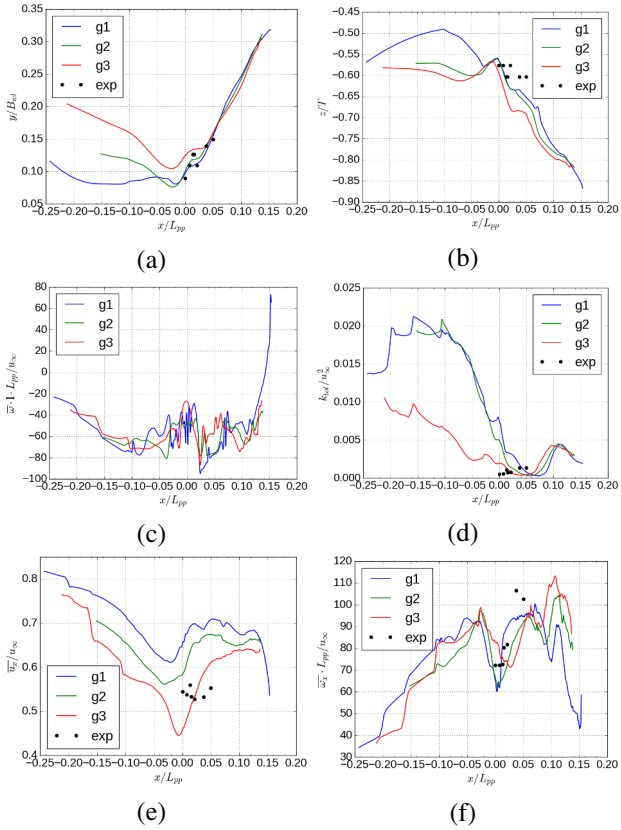

Figure 20: Sampling of the flow quantities along the vortex center for ABV: (a),(b) - y,z coordinates respectively, (c) - vorticity about the vortex center line ($\omega \cdot \mathbf{l}$), (d) - total TKE, (e) - axial velocity, (f) - axial vorticity

Physical aspects The computed values of TKE in the core of FSV have maxima in the proximity of the boundary layer (in the fore body) and quickly drop as soon as the vortex moves farther from the hull. This is probably due to insufficient grid resolution, suppressing the resolved turbulence, as it was previously mentioned. The increase of TKE values in the core of FSV vortex in stern region, which can be seen in Figure 19 is due to multiple reasons - first the adverse pressure gradient which destabilizes the vortex, second - the interaction with ABV and third - the increase of mesh resolution in that region. In addition, the trajectory of the FSV moves closer to the wake area of the hull, which is already influenced by the high turbulence level of the ship wake. One can see the increase of the longitudinal velocity of the vortex core in the regions of hull form curvature (aft shoulder) and then the decrease as the vortex approaches the stagnation region.

The strength of the ABV vortex also drops as the stagnation region is approached, but quickly increases again after that (Fig. 20). The longitudinal velocity shows minima in the stagnation region and increases after that. Values of the TKE in the ABV core rapidly grow downstream from the onset region and reach a plateau near $x = -0.1/L_{pp}$.

CONCLUSIONS

Based on the analysis of the results of the two considered cases the following main conclusions can be drawn:

1. For the straight ahead motion, RANS is more reliable for the prediction of the forces, compared to DDES. Even though the grid convergence could not be formally obtained for any of the methods, the scatter in the RANS results is less than 1%. The DDES solution on coarser grids show results consistent with the RANS ones, which corresponds to the idea of the DDES method. However, starting from some particular cell size the delay function f_d is not able to prevent the reduction of the turbulent viscosity levels upstream of the separation in the stern region. The delay function "dissolves" in response to grid refinement. This intensifies the separation due to the modelled stress depletion (MSD) and results in the increase of viscous pressure resistance on the fine mesh, giving a 4% scatter in the forces. The MSD leads not only to the inconsistencies in the force predictions, but also has consequences for the distributed quantities. The high values of the resolved TKE, observed on the fine mesh do not agree with the experimental results, whereas on the coarser grids, the agreement is substantially better. Therefore it can be concluded, that for the straight ahead motion, where the relatively weak separations are observed the DDES method suffers from the implicit (through turbulent viscosity) dependence of the shielding function to grid refinement. This dependence obviously ruins the grid convergence. Thus, the same model flaws are found, as mentioned in (Menter, 2016). The grid convergence will be very hard to attain, unless these issues are solved.

2. For the static drift condition, the forces and moments predicted by DDES showed trend to convergence. Presumably the difference to the straight ahead motion is due to stronger and well-defined separations. The grey area influence on the forces is not as pronounced in this scenario and therefore the dependence of the shielding function on the grid refinement does not play a significant role. However, for the TKE, the same conclusions can be drawn, as for the straight course. The values of the resolved TKE on the fine mesh are a few times higher, than those observed in experimental results. The distribution of the flow quantities is also smoothed in regions of high TKE, which has a negative impact on the agreement with the experiment.

3. The predicted positions of the main dominant vortices (FSV, ABV) for static drift show grid convergence and agree well ($\approx 5\%$ discrepancy) with available experimental data. The values of k and ω_x in the core of the vortex are considerably more sensitive to grid refinement and in most cases diverging solutions are observed: agreement of these quantities with their experimentally obtained counterparts is poor in majority of the cases. For the vortex onset, the discrepancies are smaller, since RANS is used in the onset region, but grid refinement decreases the prediction accuracy. Presumably, a finer grid is required for the resolution of the vortices to reach an asymptotic range. However, care should be taken, not to refine the mesh at the vicinity of the ship as well, because of the dependence of the shielding function on the cell size.

4. The development of a delay function or a simulation approach, preserving the total TKE levels in the proximity of the wall regardless of the grid refinement and at the same time not suppressing unsteady fluctuations in the wake regions is considered a major challenge for further studies.

ACKNOWLEDGEMENTS

The authors sincerely thank Prof. Nikolai Kornev and Prof. Michel Visonneau for providing a valuable feedback to our paper and Prof. Frederick Stern for fruitful discussions. This research would have been impossible without the financial support provided by the German Federal Ministry for Economic Affairs and Energy under the grant 03SX488B (investigation of the turbulent flow of the Japan Bulk Carrier (JBC)) and the partial funding awarded by the Office of Naval Research Global, Grant N62909-18-1-2080, under the administration of Drs. Woei-Min Lin, Salahuddin Ahmed, Patrick Rose and Elena McCarthy.

REFERENCES

Abdel-Maksoud, M., Müller, V., Xing, T., Toxopeus, S., Stern, F., Petterson, K., Tormalm, M., Kim, S., Aram, S., Gietz, U., *et al.*, "Experimental and Numerical Investigations on Flow Characteristics of the KVLCC2 at 30 Drift Angle", 5th World Maritime Technology Conference, November, 2015, pp. 3–7.

Bhushan, S., Alam, M., & Walters, D., "Evaluation of hybrid RANS/LES models for prediction of flow around surface combatant and Suboff geometries ", Computers & Fluids, Vol. 88, 2013, pp. 834–849.

Deng, G., Leroyer, A., Guilmineau, E., Queutey, P., Visonneau, M., Wackers, J., & del Toro Llorens, A., "Verification and Validation of Resistance and Propulsion Computation", Tokyo 2015 - A Workshop on CFD in Ship Hydrodynamics, 2015, pp. 261–266.

Feder, D.F., Shevchuk, I., Sahab, A., Gerwers, L., & Abdel-Maksoud, M., "Fore-Body Side Vortex of KVLCC2 at 30 Degree Drift: A Trailing Vortex Resolved with DES and Compared to PIV Data", Open Journal of Fluid Dynamics, Vol. 09, No. 04, 2019, pp. 303–325.

Fröhlich, J. & von Terzi, D., "Hybrid LES/RANS Methods for the Simulation of Turbulent Flows", Progress in Aerospace Sciences, Vol. 44, 2008, pp. 349–377.

Fureby, C., Toxopeus, S., Johansson, M., Tormalm, M., & Petterson, K., "A computational study of the flow around the KVLCC2 model hull at straight ahead conditions and at drift", Ocean Engineering, Vol. 118, 2016, pp. 1–16.

Gritskevich, M., Garbaruk, A., Schütze, J., & Menter, F., "Development of DDES and IDDES Formulations for the k-ω Shear Stress Transport Model", Flow, Turbulence and Combustion, Vol. 88, No. 3, 2011, pp. 431–449.

Ismail, F., Carrica, P.M., Xing, T., & Stern, F., "Evaluation of linear and nonlinear convection schemes on multidimensional non-orthogonal grids with applications to KVLCC2 tanker", International Journal for Numerical Methods in Fluids, 2009, pp. n/a–n/a.

ITTC, "Recommended Procedures and Guidelines. 7.5-01-01-01. Ship Models", 2017.

Larsson, L., Stern, F., Visonneau, M., Hirata, N., Hino, T., & Kim, J., eds., Tokyo 2015 - A Workshop on CFD in Ship Hydrodynamics, 2015.

Menter, F., "Stress-Blended Eddy Simulation (SBES) – A New Paradigm in Hybrid RANS-LES Modeling.", Progress in Hybrid RANS-LES Modelling: Papers Contributed to the 6th Symposium on hybrid RANS-LES Methods, 2016.

Merlet, J.P., "Kinematics of the wire-driven parallel robot MARIONET using linear actuators", Robotics and Automation, 2008. ICRA 2008. IEEE International Conference on, IEEE, 2008, pp. 3857–3862.

Mockett, C., Fuchs, M., Garbaruk, A., Shur, M., Spalart, P., Strelets, M., Thiele, F., & Travin, A., Progress in Hybrid RANS-LES Modelling: Papers Contributed to the 5th Symposium on Hybrid RANS-LES Methods, 19-21 March 2014, College Station, A&M University, Texas, USA, chap. Two Non-zonal Approaches to Accelerate RANS to LES Transition of Free Shear Layers in DES, Springer International Publishing, Cham, 2015, pp. 187–201.

Sagaut, P., Deck, S., & Terracol, M., Multiscale and Multiresolution Approaches in Turbulence: LES, DES and Hybrid RANS/LES Methods: Applications and Guidelines, Imperial College Press, 2013.

Shima, E., Kitamura, K., & Haga, T., "Green-Gauss/Weighted-Least-Squares Hybrid Gradient Reconstruction for Arbitrary Polyhedra Unstructured Grids", AIAA Journal, Vol. 51, No. 11, 2013, pp. 2740–2747.

Spalart, P.R., "Strategies for turbulence modelling and simulations", International Journal of Heat and Fluid Flow, Vol. 21, No. 3, 2000, pp. 252–263.

Spalart, P.R., Deck, S., Shur, M.L., Squires, K.D., Strelets, M.K., & Travin, A., "A New Version of Detached-eddy Simulation, Resistant to Ambiguous Grid Densities", Theoretical and Computational Fluid Dynamics, Vol. 20, No. 3, 2006, pp. 181–195.

Strelets, M., Detached eddy simulation of massively separated flows, Aerospace Sciences Meetings, American Institute of Aeronautics and Astronautics, 2001.

Sujudi, D. & Haimes, R., "Identification of swirling flow in 3-D vector fields", In 12th Computational Fluid Dynamics Conference, 1995.

Visonneau, M., Deng, G.B., Guilmineau, E., Queutey, P., & Wackers, J., "Local and Global Assessment of the Flow around the Japan Bulk Carrier with and without Energy Saving Devices at Model and Full Scale", Proceedings of the 31th Symposium on Naval Hydrodynamics, 2016, pp. 1–20.

Visonneau, M., Guilmineau, E., & Rubino, G., "Computational Analysis of the Flow Around a Surface Combatant at 10deg Static Drift and Dynamic Sway Conditions", Proceedings of the 32nd Symposium on Naval Hydrodynamics, 2018.

Xing, T., Bhushan, S., & Stern, F., "Vortical and turbulent structures for KVLCC2 at drift angle 0, 12, and 30 degrees", Ocean Engineering, Vol. 55, 2012, pp. 23–43.

Yin, Z., Reddy, K.R., & Durbin, P.A., "On the dynamic computation of the model constant in delayed detached eddy simulation", Physics of Fluids, Vol. 27.

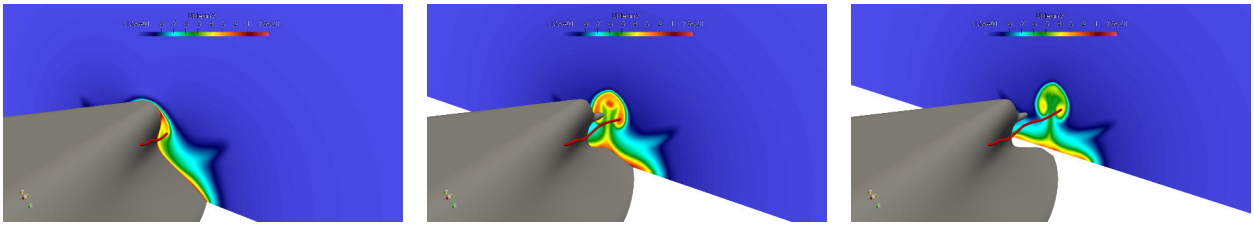

(x/L_{pp} = 0.05) (x/L_{pp} = 0.0) (x/L_{pp} = -0.03)

Figure 21: Comparison of u_x distribution at three sections

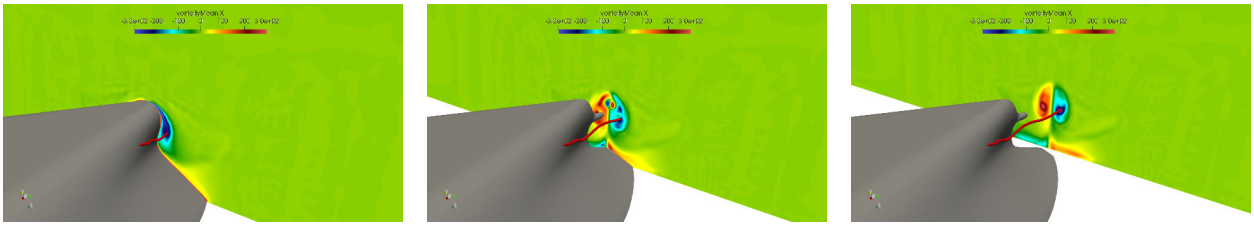

(x/L_{pp} = 0.05) (x/L_{pp} = 0.0) (x/L_{pp} = -0.03)

Figure 22: Comparison of ω_x distribution at three sections

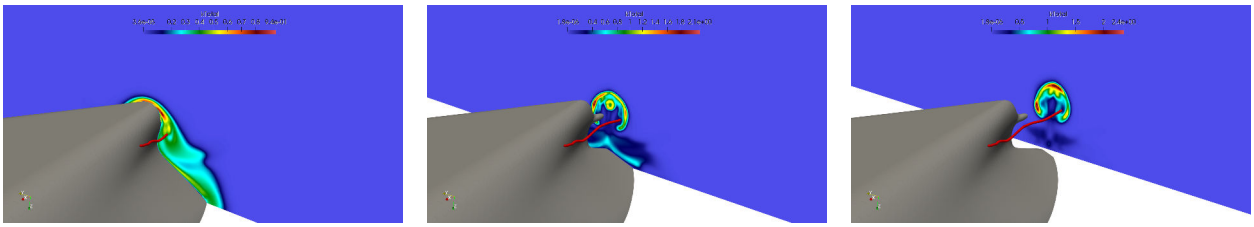

(x/L_{pp} = 0.05) (x/L_{pp} = 0.0) (x/L_{pp} = -0.03)

Figure 23: Comparison of k_{tot} distribution at three sections

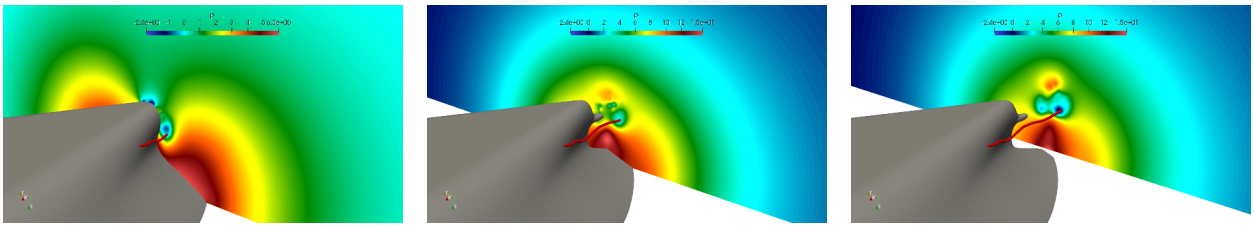

(x/L_{pp} = 0.05) (x/L_{pp} = 0.0) (x/L_{pp} = -0.03)

Figure 24: Comparison of p distribution at three sections

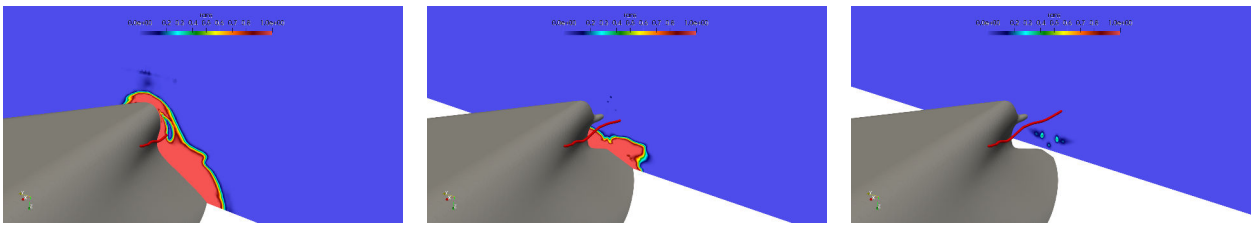

(x/L_{pp} = 0.05) (x/L_{pp} = 0.0) (x/L_{pp} = -0.03)

Figure 25: Comparison of f_d distribution at three sections

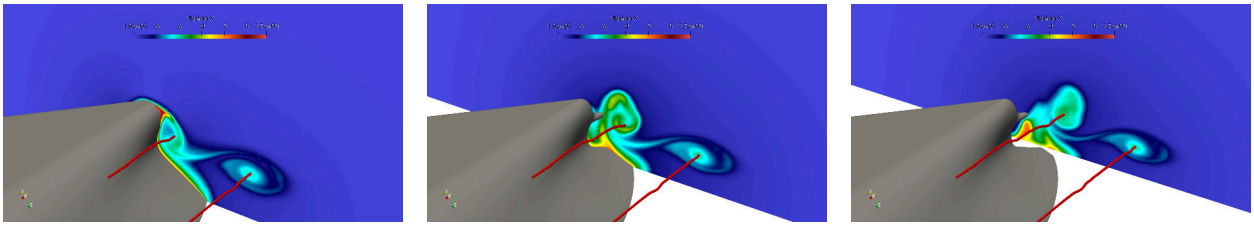

(x/L_{pp} = 0.05) (x/L_{pp} = 0.0) (x/L_{pp} = -0.03)

Figure 26: Comparison of u_x distribution at three sections

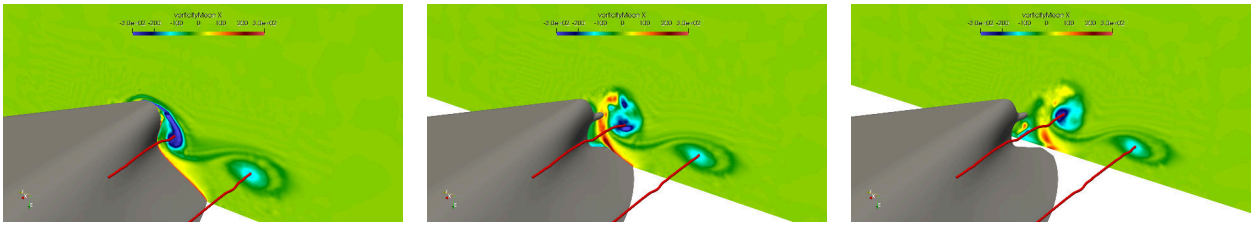

(x/L_{pp} = 0.05) (x/L_{pp} = 0.0) (x/L_{pp} = -0.03)

Figure 27: Comparison of ω_x distribution at three sections

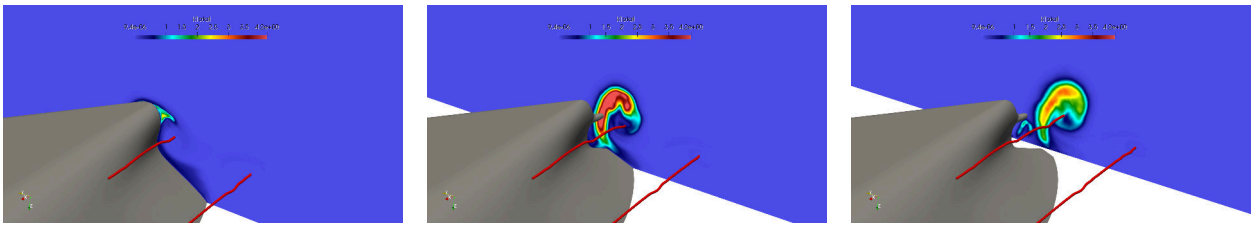

(x/L_{pp} = 0.05) (x/L_{pp} = 0.0) (x/L_{pp} = -0.03)

Figure 28: Comparison of k_{tot} distribution at three sections

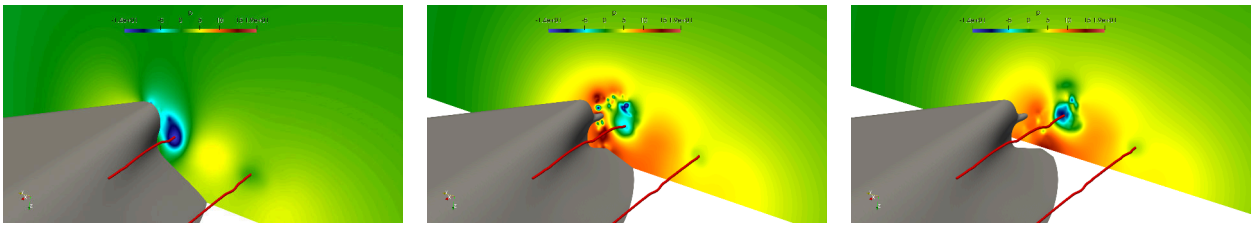

(x/L_{pp} = 0.05) (x/L_{pp} = 0.0) (x/L_{pp} = -0.03)

Figure 29: Comparison of p distribution at three sections

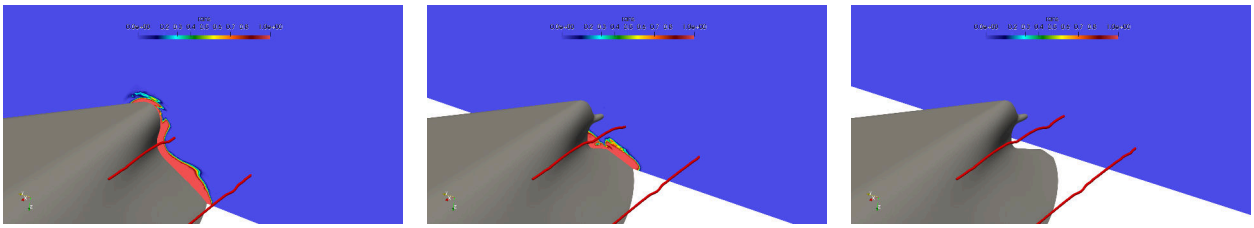

(x/L_{pp} = 0.05) (x/L_{pp} = 0.0) (x/L_{pp} = -0.03)

Figure 30: Comparison of f_d distribution at three sections

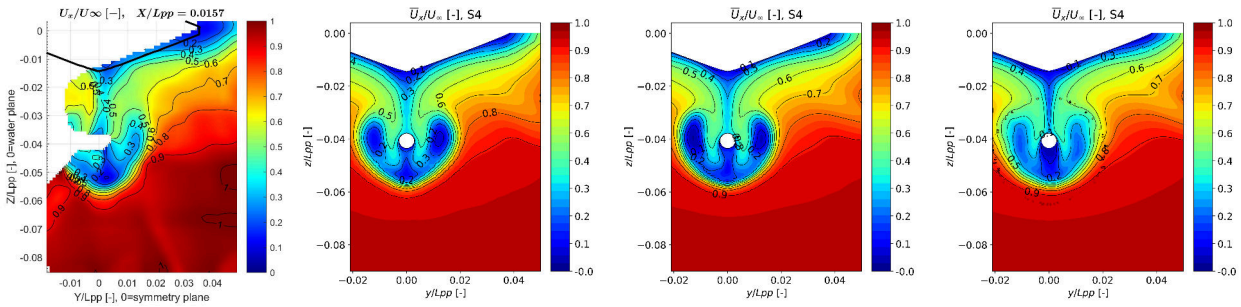

(exp) (coarse) (medium) (fine)

Figure 31: Comparison of the u_x distribution at section S4, TUHH, DDES

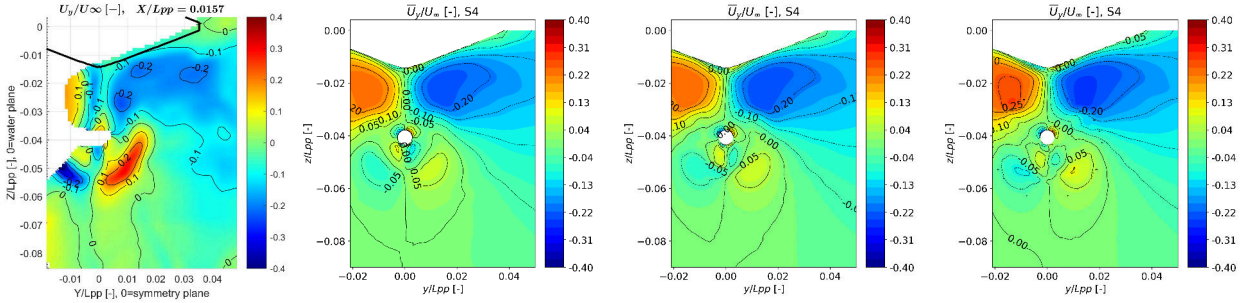

(exp) (coarse) (medium) (fine)

Figure 32: Comparison of the u_y distribution at section S4, TUHH, DDES

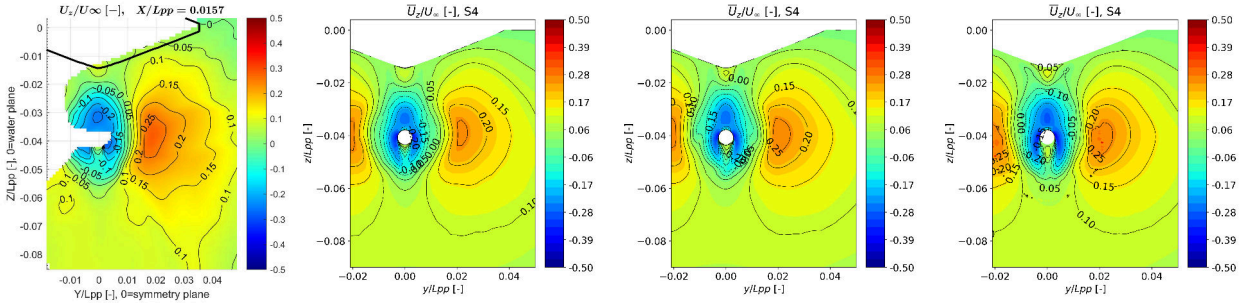

(exp) (coarse) (medium) (fine)

Figure 33: Comparison of the u_z distribution at section S4, TUHH, DDES

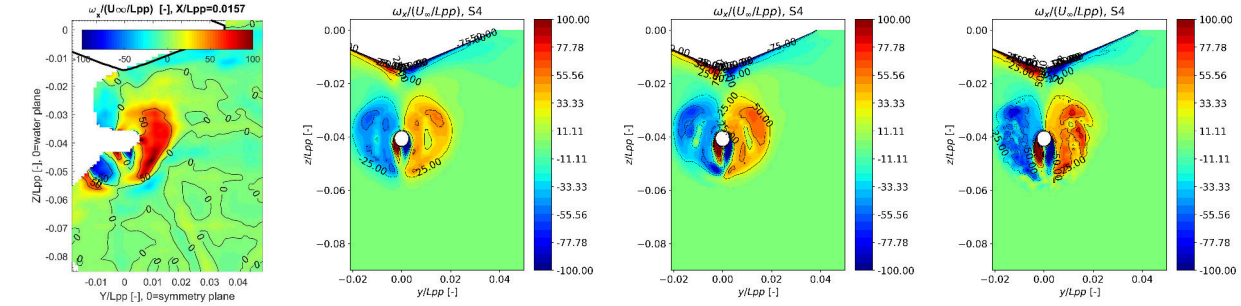

(exp) (coarse) (medium) (fine)

Figure 34: Comparison of the ω_x distribution at section S4, TUHH, DDES

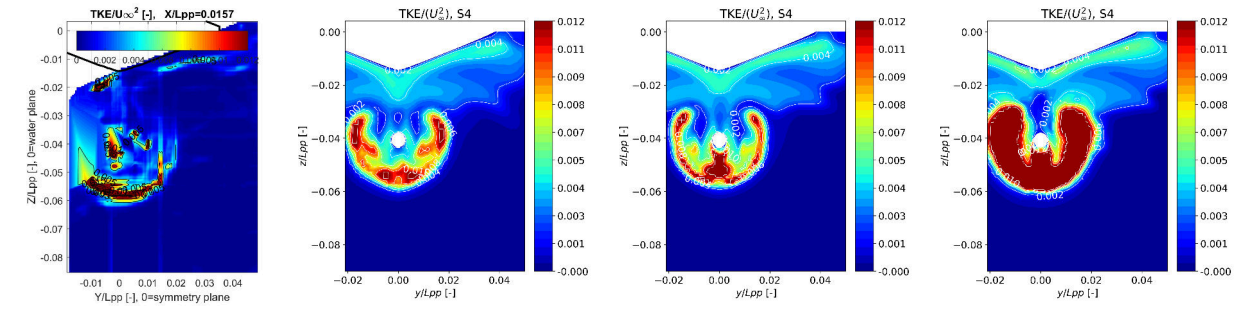

(exp) (coarse) (medium) (fine)

Figure 35: Comparison of the k_{tot} distribution at section S4, TUHH, DDES

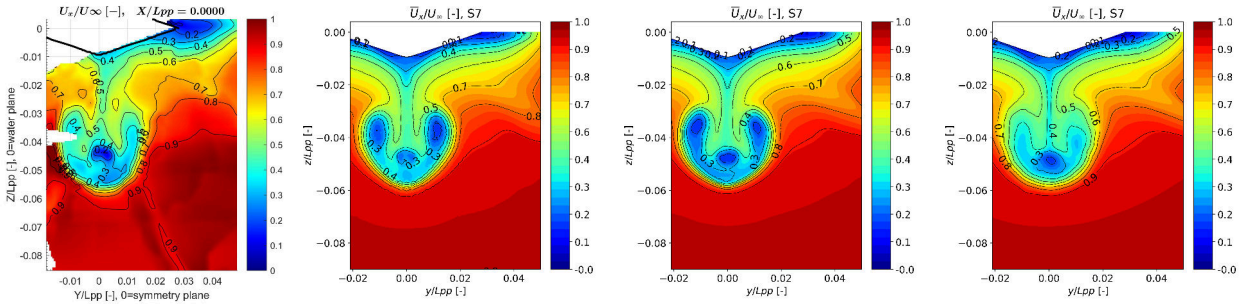

(exp) (coarse) (medium) (fine)

Figure 36: Comparison of the u_x distribution at section S7, TUHH, DDES

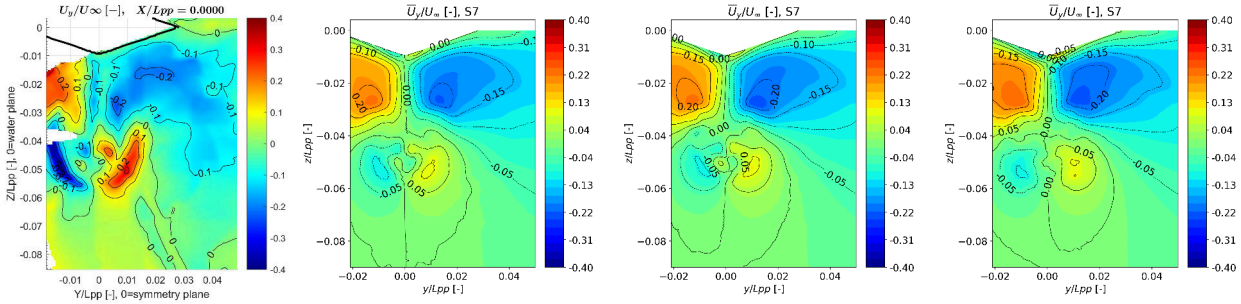

(exp) (coarse) (medium) (fine)

Figure 37: Comparison of the u_y distribution at section S7, TUHH, DDES

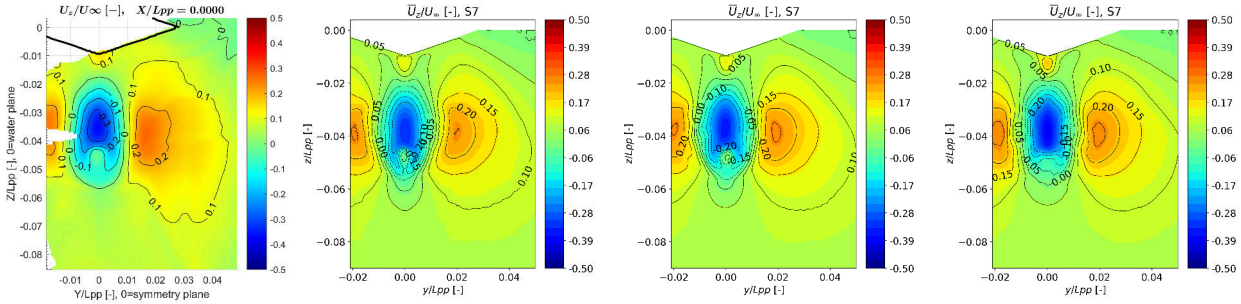

(exp) (coarse) (medium) (fine)

Figure 38: Comparison of the u_z distribution at section S7, TUHH, DDES

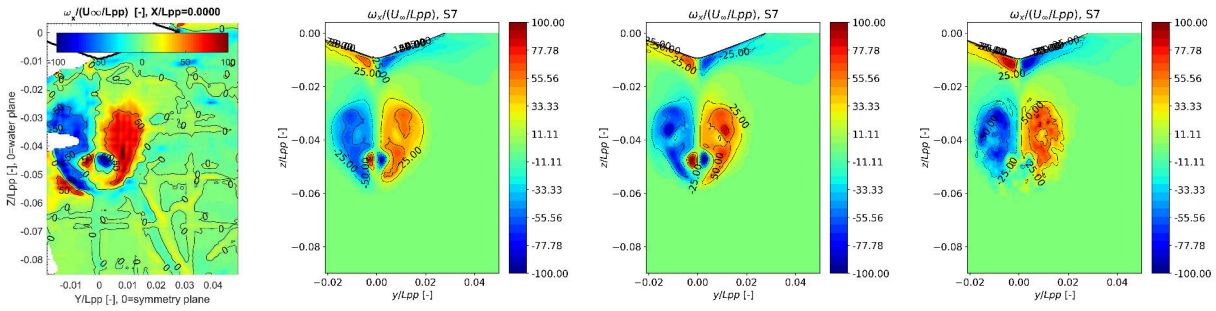

(exp) (coarse) (medium) (fine)

Figure 39: Comparison of the ω_x distribution at section S7, TUHH, DDES

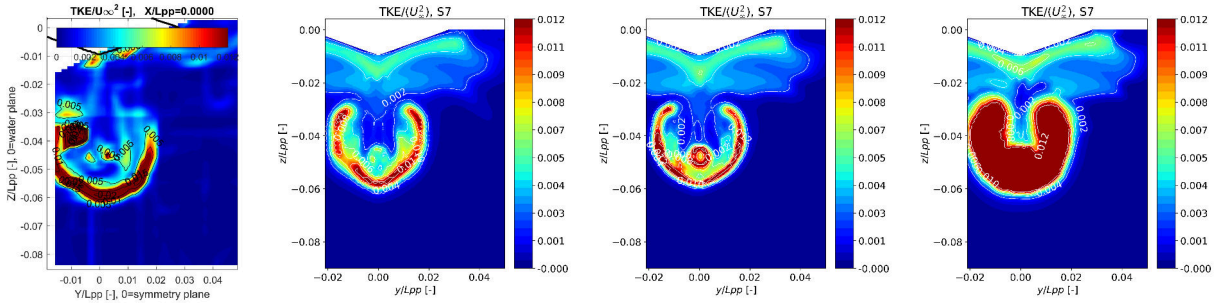

(exp) (coarse) (medium) (fine)

Figure 40: Comparison of the k_{tot} distribution at section S7, TUHH, DDES

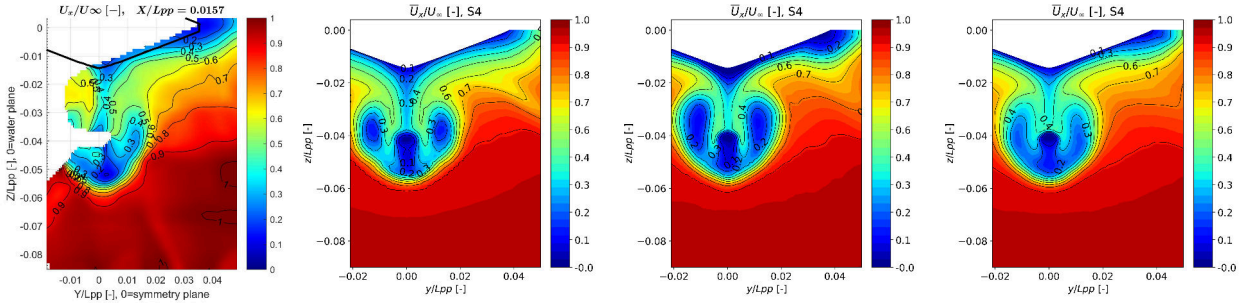

(exp) (coarse) (medium) (fine)

Figure 41: Comparison of the u_x distribution at section S4, TUHH, Dynamic DDES

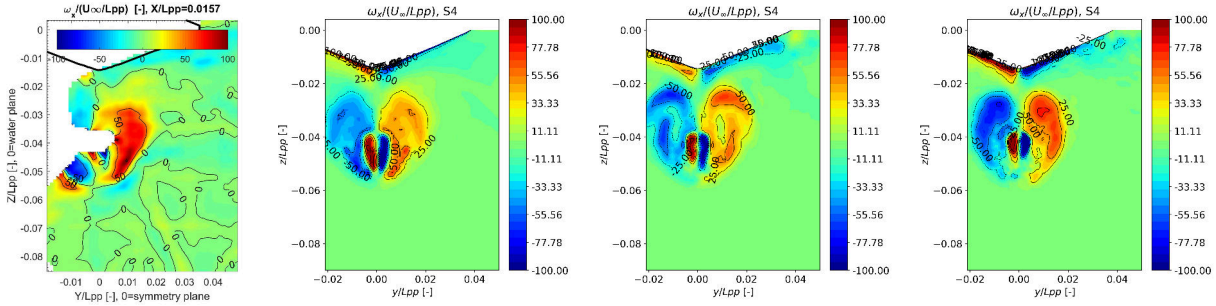

(exp) (coarse) (medium) (fine)

Figure 42: Comparison of the ω_x distribution at section S4, TUHH, Dynamic DDES

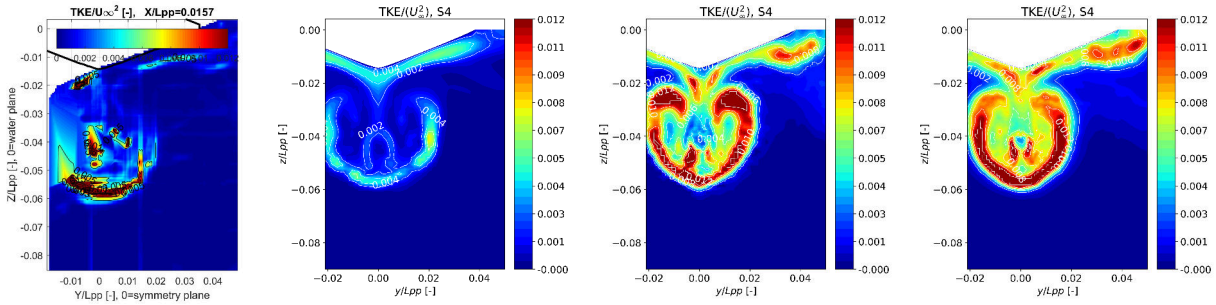

(exp) (coarse) (medium) (fine)

Figure 43: Comparison of the k_{tot} distribution at section S4, TUHH, Dynamic DDES

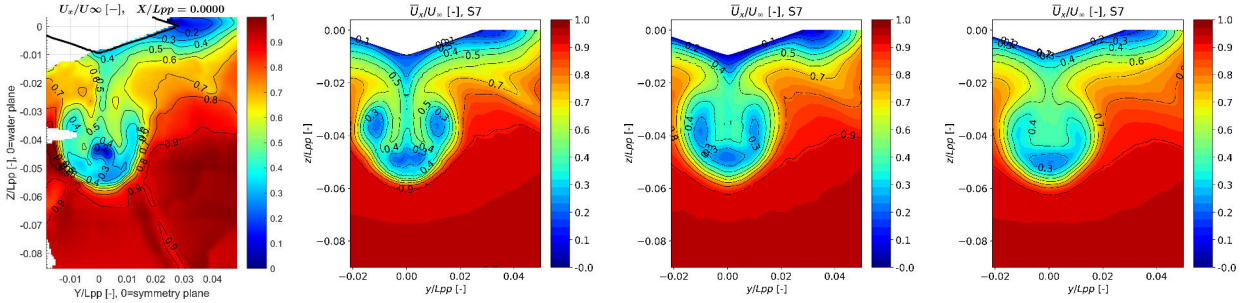

(exp) (coarse) (medium) (fine)

Figure 44: Comparison of the u_x distribution at section S7, TUHH, Dynamic DDES

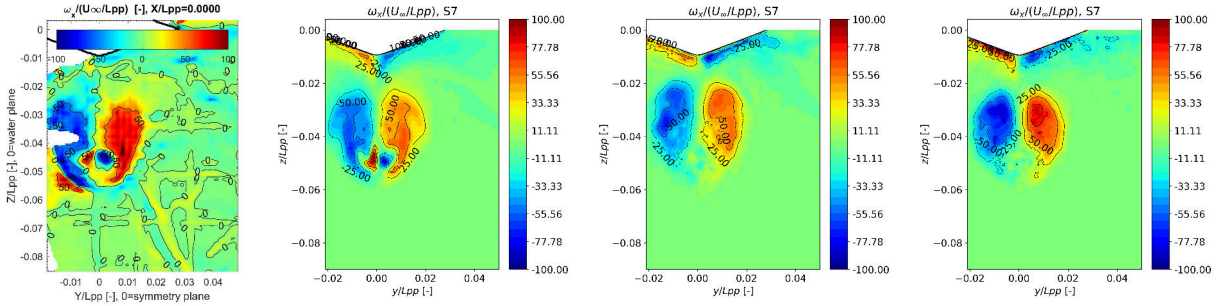

(exp) (coarse) (medium) (fine)

Figure 45: Comparison of the ω_x distribution at section S7, TUHH, Dynamic DDES

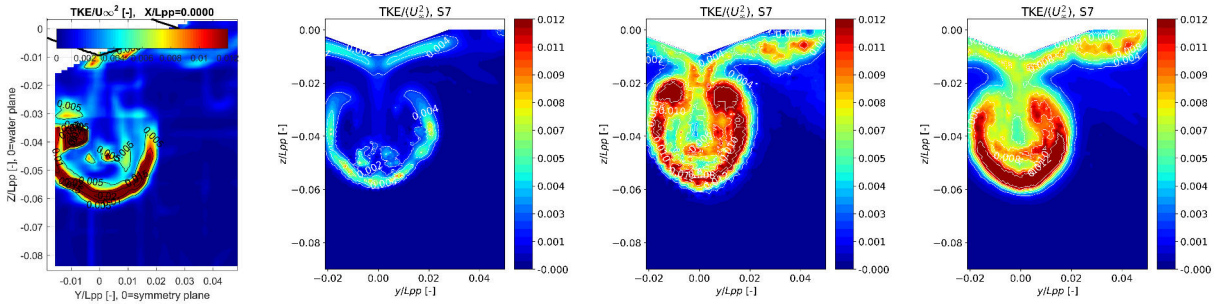

(exp) (coarse) (medium) (fine)

Figure 46: Comparison of the k_{tot} distribution at section S7, TUHH, Dynamic DDES

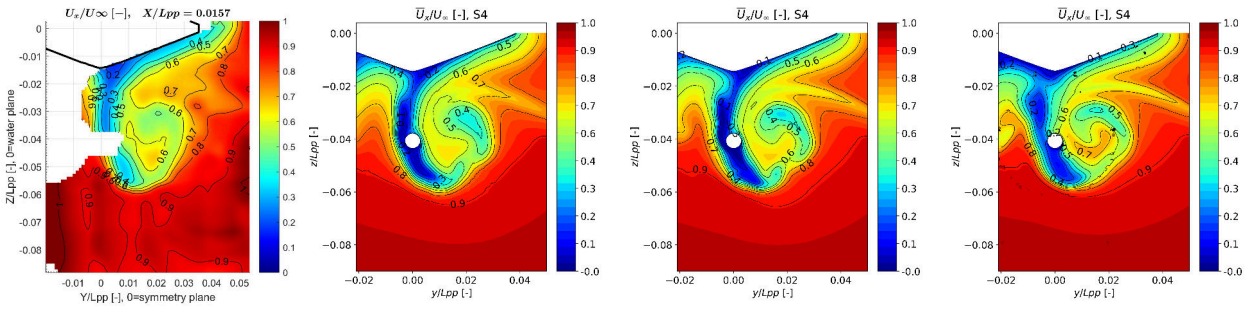

(exp) (coarse) (medium) (fine)

Figure 47: Comparison of the u_x distribution at section S4, TUHH, DDES

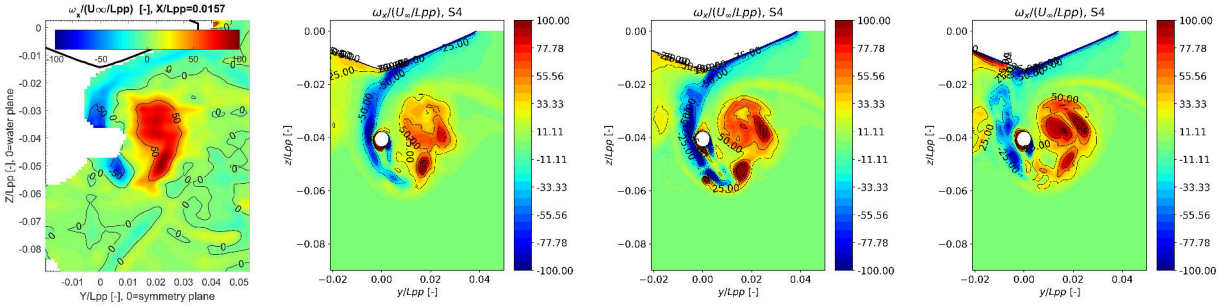

(exp) (coarse) (medium) (fine)

Figure 48: Comparison of the ω_x distribution at section S4, TUHH, DDES

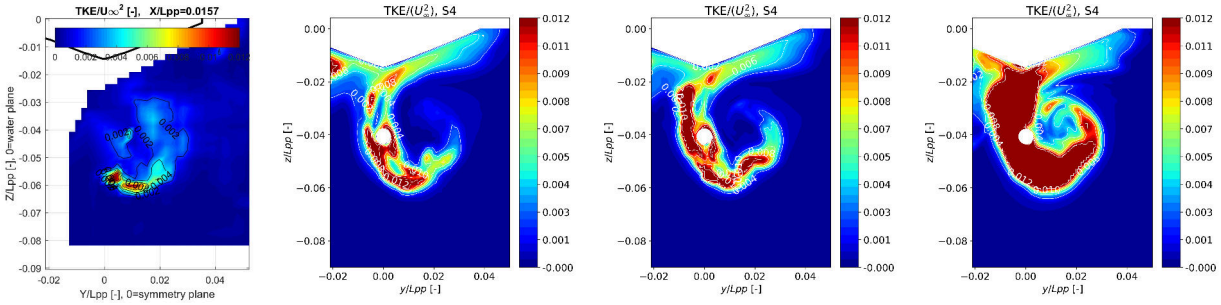

(exp) (coarse) (medium) (fine)

Figure 49: Comparison of the k_{tot} distribution at section S4, TUHH, DDES

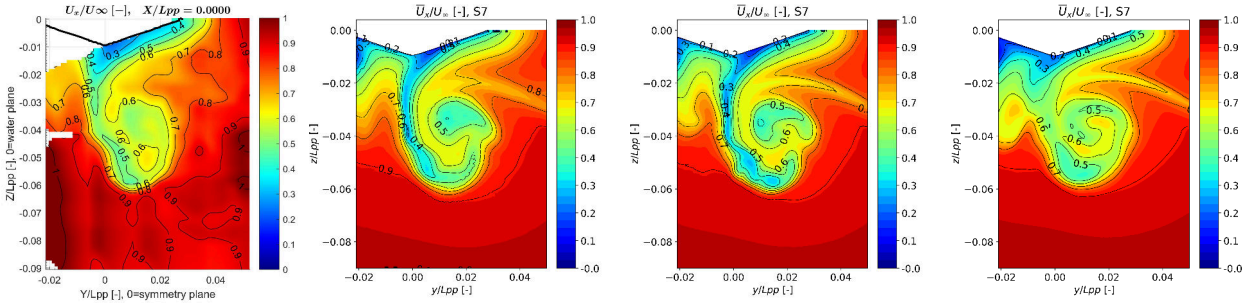

(exp) (coarse) (medium) (fine)

Figure 50: Comparison of the u_x distribution at section S7, TUHH, DDES

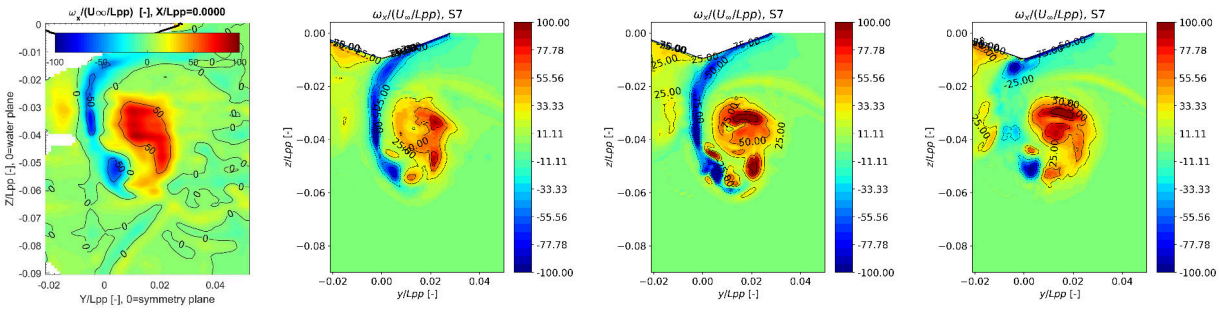

(exp) (coarse) (medium) (fine)

Figure 51: Comparison of the ω_x distribution at section S7, TUHH, DDES

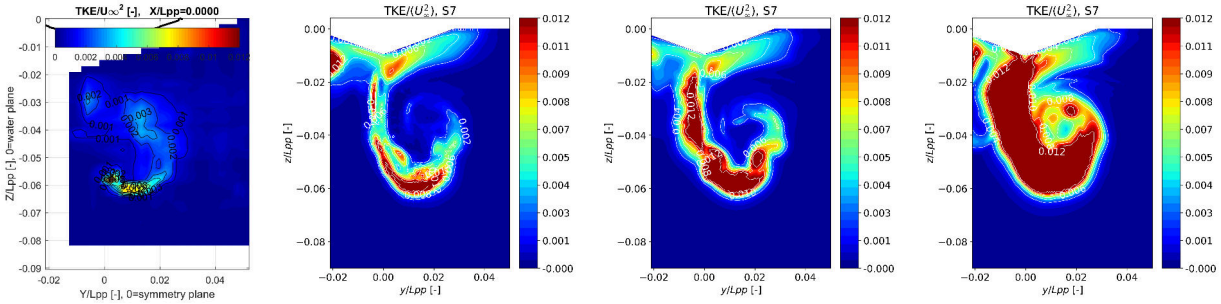

(exp) (coarse) (medium) (fine)

Figure 52: Comparison of the k_{tot} distribution at section S7, TUHH, DDES

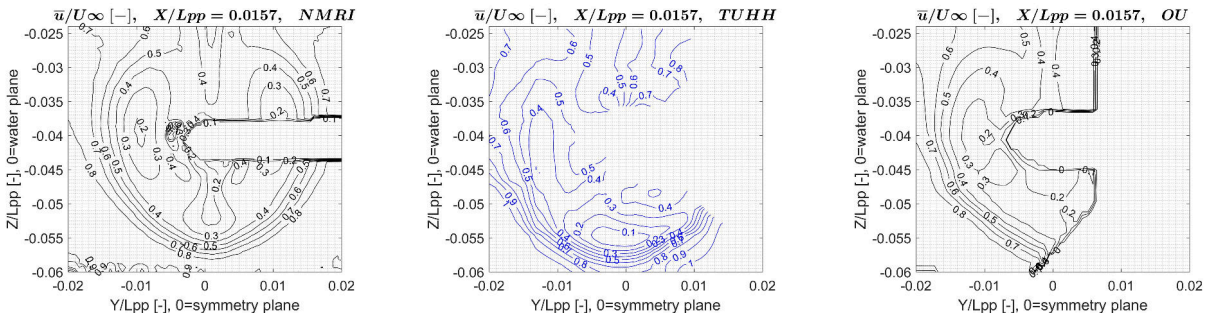

(a) (b) (c)

Figure 53: NMRI (a), TUHH (b), OU (c) results for u_x at S4

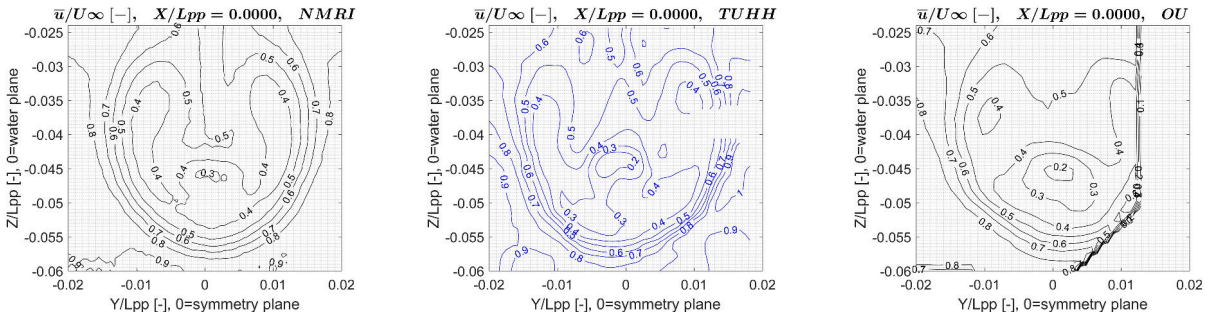

(a) (b) (c)

Figure 54: NMRI (a), TUHH (b), OU (c) results for u_x at S7

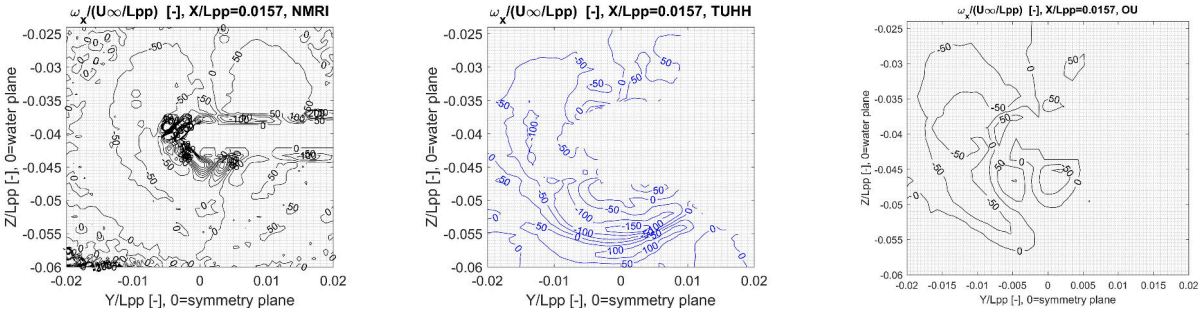

(a) (b) (c)

Figure 55: NMRI (a), TUHH (b), OU (c) results for ω_x at S4

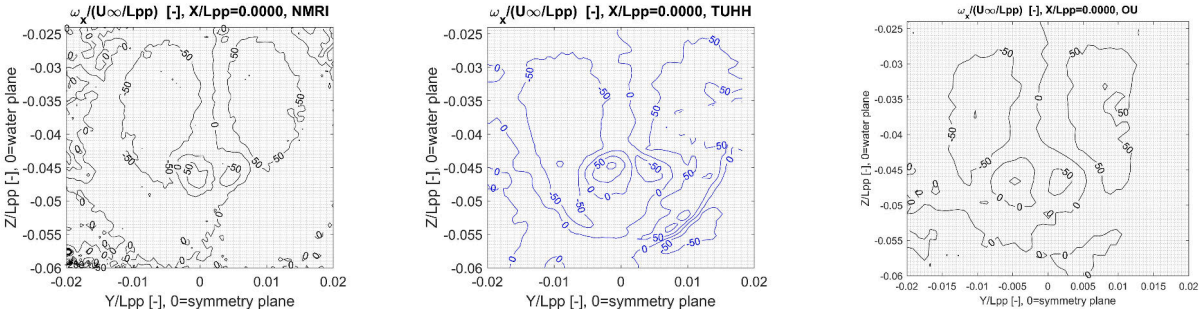

(a) (b) (c)

Figure 56: NMRI (a), TUHH (b), OU (c) results for ω_x at S7

DISCUSSION

Prof. Nikolai Kornev, University of Rostock, Germany

The authors presented a very interesting and comprehensive work including both the experiment and numerical CFD simulations. The paper shows that the determination of the wake behind full ships especially its unsteady parameters remains a very challenging topic. The discrepancy between data is documented between different experiments (Osaka versus TUHH measurements), different models (RANS, DDES and dynamic DDES) as well as between experiment and theory. The proof of new version of the DDES model, the dynamic one, is an important result of this paper. Generally, I agree with the author's conclusions with exception for the prospect of searching for a shielding function which would solve the gray zone problem in hybrid methods. The authors show a strong influence of the grid resolution on the determination of the TKE which is in accordance with my experience.

Question 1. Do they have data showing the influence of the time step on the TKE? Did they prove that the time average period is sufficient for the gathering the statistical data both in the simulations (three ship length path) and in measurement (1000 images)?

Question 2. The authors explained very convincingly the divergence of the TKE with increase of resolution by the deterioration of shielding properties of the DDES delay function on finer meshes. Additionally, It would be interesting to know why the velocity u_z is predicted relatively well, whereas the transversal component u_y not. Does it relate to the structure of the vortex which is rather intermittent in simulations (consists of many sub vortices) whereas it is more solid in measurements? How to explain such an intermittency? Why the vortex in the dynamic DDES model is less intermittent than in the DDES one? Does it lead to the improvement of results for u_y?

Despite the many shortcomings of hybrid methods shown in the present work, which may cause some skepticism, there is no alternative for hybrid methods when the unsteady flow parameters of the ship wake should be studied.

Prof. Michel Visonneau, ECN, France

Nice paper on the computation of the viscous flow around JBC with RANS and Hybrid RANS/LES turbulence models. One notices a very large difference on the force evaluation between DDES (in good agreement with RANS) and Dynamic DDES (Table 4).

Question 3. It would be interesting to give an explanation or to show the longitudinal distribution of forces to detect the longitudinal location of the differences.

Anyway, Figure 11 shows that the shielding implemented in Dyn-DDES is ineffective. Disappointing results are shown with the grid refinement but one should remind that the straight ahead case is the most difficult in terms of tke prediction. Same behavior was observed on the DTMB5415 in straight ahead condition. Moreover, it is impossible to conduct a rigorous grid refinement study with DDES, particularly because of the shielding function which will not behave in the same way for the various considered grids.

Question 4. Some additional information would be welcome like a local comparison of the grid cell size in the vortex core with Taylor scale. Tke spectrum in the core of the vortex would also be valuable for DDES and Dyn-DDES. Globally, this interesting paper complies with the SNH standards.
Typos: Reference section : compuational

AUTHOR'S REPLY

Reply 1. The statistical convergence of the experimental results was analysed for the longitudinal velocity component at the point (y/L_{pp}, z/L_{pp}) = 0.05, -0.035. One can see that the statistical convergence is attained already with 800 snapshots with only slight variations between 800 and 1000 (see Fig. 57). The statistical convergence of

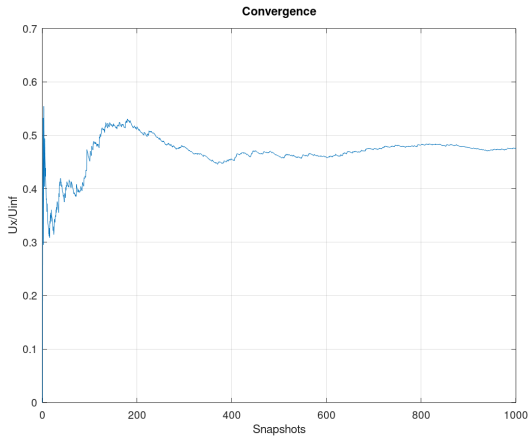

Figure 57: Statistical convergence of the experimental data

the computational results was not verified for this particular case. The dimensionless averaging time was chosen based on the hybrid RANS/LES simulation experience for similar ship flows.

We would like to present here the convergence analysis results for a flow around a ship with 11m length, with the incident flow velocity of 1.24 m/s. The flow was simulated using SST-IDDES. The averaging time was varied from 3s to 9s with a step of 3s. In the plots below you can see the convergence of the longitudinal velocity profile along a line in the ship wake for different averaging periods: mean value and the standard deviation. One

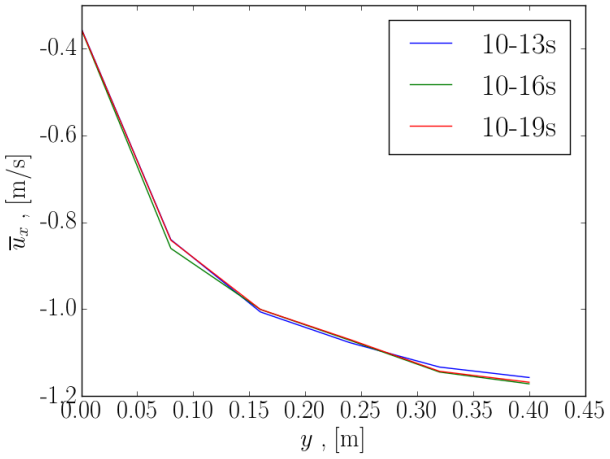

Figure 58: Statistical convergence of the computational data, $\overline{u}$

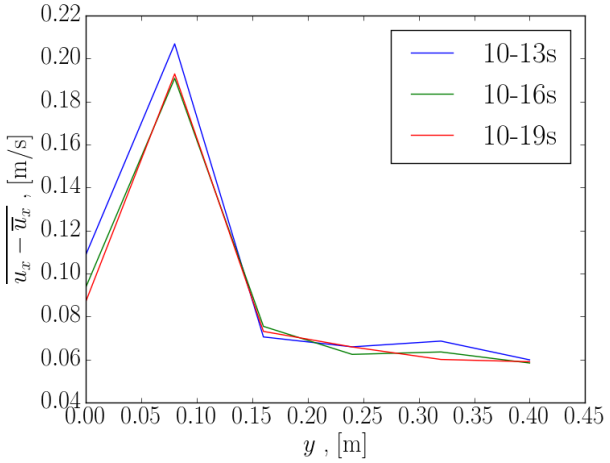

Figure 59: Statistical convergence of the computational data, $\overline{u'}$

can notice (see Fig. 58), that the mean value converges already after flow passes 33% of the ship length, whereas the convergence of standard deviation obviously needs more time (see Fig. 59), but can be achieved after flow passes one ship length (9 s). In order to be on the "safe side", in the computations of JBC we increased the dimensionless averaging time $(Ut)/L$ to 3.

Reply 2. We believe, that the reason, why the agreement for u_y is so poor below the stern bulb is that this is the region where the boundary layer rolls up in the ABV vortex (see Figure 34). The vortices of the energy containing range might be very small in this thin shear layer. In RANS this flow feature is smeared because of isotropic viscosity. Whereas in hybrid simulations we are probably not able to resolve the most relevant turbulent scales in this exact region, because the mesh is too coarse. However, as the mesh is refined one can see a slight improvement in ω_x below the stern bulb. Unfortunately, further grid refinement supposedly won't bring any improvement because of GIS. We are going to investigate this issue further.

Reply 3. We added the Figure 9, showing the longitudinal distribution of the averaged force coefficient for different meshes. One can see a difference in C_p distribution in the stern region between g1 and g2,g3, resulting from the GIS.

Reply 4. We added the information regarding the Taylor microscales to the "Mesh generation" subsection. Unfortunately, in order to plot the TKE spectrum, a new simulation had to be started, which was not feasible. But since the resolution of the values in the core of FSV vortex was not the aim of the work and therefore the mesh was quite coarse, one can expect that the energy spectrum in the vortex core is erroneous in our simulations with almost no resolved fluctuations.